J. Fluid Mech. (2002), *vol.* 464, *pp.* 81–111.
DOI: 10.1017/S0022112002001015 Printed in the United Kingdom

Turbulent convection driven by surface cooling in shallow water

By OLEG ZIKANOV[1], DONALD N. SLINN[2] AND MANHAR R. DHANAK[3]

[1]Department of Mechanical Engineering, University of Michigan – Dearborn, Dearborn, MI 48128-1491, USA

[2]Department of Civil and Coastal Engineering, University of Florida, Gainesville, FL 32611-6590, USA

[3]Department of Ocean Engineering, Florida Atlantic University, Boca Raton, FL 33431-0991, USA

(Received 21 May 2001 and in revised form 13 February 2002)

We present the results of large-eddy simulations (LES) of turbulent thermal convection generated by surface cooling in a finite-depth stably stratified horizontal layer with an isothermal bottom surface. The flow is a simplified model of turbulent convection occurring in the warm shallow ocean during adverse weather events. Simulations are performed in a $6 \times 6 \times 1$ aspect ratio computational domain using the pseudo-spectral Fourier method in the horizontal plane and finite-difference discretization on a high-resolution clustered grid in the vertical direction. A moderate value of the Reynolds number and two different values of the Richardson number corresponding to a weak initial stratification are considered. A version of the dynamic model is applied as a subgrid-scale (SGS) closure. Its performance is evaluated based on comparison with the results of direct numerical simulations (DNS) and simulations using the Smagorinsky model. Comprehensive study of the spatial structure and statistical properties of the developed turbulent state shows some similarity to Rayleigh–Bénard convection and other types of turbulent thermal convection in horizontal layers, but also reveals distinctive features such as the dominance of a large-scale pattern of descending plumes and strong turbulent fluctuations near the surface.

1. Introduction

In this paper we report results of numerical simulations of turbulent convection generated by surface cooling in a layer of finite depth. The flow is a model of the geophysical phenomenon that occurs in warm littoral waters in response to a cold air outbreak.

The passage of a cold atmospheric front over tropical waters, such as off South Florida, can cause a sudden (within few hours) drop of air temperature by as much as 10 °C. During the following few days, the air remains considerably (several degrees) colder than the ocean water. An example of the recorded temperature series is shown in figure 1. Helped by radiative cooling due to, typically, clear skies, this leads to significant convectively driven motions in the shallow water column. Field measurements during such events show significant turbulent mixing and enhanced rates of kinetic energy dissipation in areas with depths up to 15 m.

During the passage of the front, the accompanying winds, over the initial period,

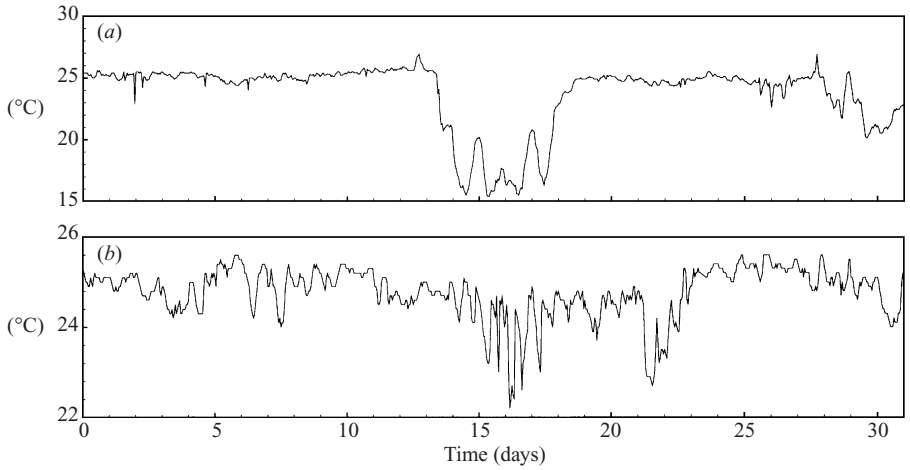

FIGURE 1. Typical atmospheric and ocean conditions during an adverse weather event. Air (*a*) and water surface (*b*) temperatures are shown as measured by a FWFY NOAA E-MAN buoy in December 1998 at approximately 26°3.58′ N and 80°5.58′ W (continental shelf off Fort Lauderdale, Florida). A cold spell in the middle of the month is the result of the passage of a cold atmospheric front.

blow offshore (An *et al.* 2001). The offshore fetch is often too short (hundreds of metres) to produce large-amplitude waves in the littoral zone, typically resulting in fairly flat local seas.

It is very difficult and often impossible to make accurate non-intrusive measurements of ocean flow phenomena. The measured data typically reflect a multitude of diverse effects. For the flows in littoral waters considered in this paper, inevitable complicating factors include, for example, variable bottom topography and pressure-generated mean currents. Numerical simulations of an idealized problem similar to the study we report here seem to be especially important for the ocean flows since they allow isolation and investigation of one particular phenomenon.

Here, we neglect the complicating effects mentioned above; these important issues may be included in subsequent studies. Further we assume that the diurnal oscillations of air temperature, although present, are considerably smaller than the general temperature drop and can be neglected (see figure 1*a*). Thus, the problem is simplified to that of turbulent convection generated by constant cooling applied at the surface in an initially stably stratified finite-depth horizontal layer.

The initial stratification is due to the salinity and, to a smaller degree, temperature gradients in an unperturbed fluid. The convective motions are generated solely by the buoyancy mechanisms caused by inhomogeneities of the temperature field.

The isothermal (zero density perturbations) boundary condition is applied at the bottom of the layer. This is in contrast to the no-flux condition often used for density in oceanic flows. As a justification, we notice that the no-flux condition would be unquestionably appropriate only for the density perturbations caused by variations in salinity. For the temperature-induced fluctuations, both isothermal and adiabatic conditions are idealizations of actual processes near the ocean bottom. We use the isothermal approximation in these first simulations. The effect of the bottom boundary condition will be a subject of future studies.

The flow considered in this paper belongs to the intensively studied family of thermo-convective turbulent flows in wide horizontal layers. Well-known members

of the same family are, for example, Rayleigh–Bénard flow, the planetary boundary layer, and penetrative convection caused by internal volumetric heat sources (see e.g. experiments by Kulacki & Emara 1977 and applications to the solar granulation phenomenon in Brummel, Cattaneo & Toomre 1995 and references therein). Our model is close to the experimental setup of Adrian, Ferreira & Boberg (1986, referred to herein as AFB86) where turbulent convection was generated in a layer between two rigid plates by heating the lower plate and keeping the upper plate thermally insulated.

A member of the family that stands out due to its peculiar properties is open ocean convection (see Marshall & Schott 1999 or Maxworthy 1997 for a review), which is generated by cooling of the surface of a deep stably stratified ocean. Unlike the flows mentioned above, the dynamics of deep ocean convection is typically dominated by the background stratification and the localized character of the cooling.

It has to be stressed that, despite all the similarities between the system considered in this paper and other convective layers, our system demonstrates a unique combination of the flow properties. For example, the buoyancy flux is applied at a free surface and not at a rigid wall as in Rayleigh–Bénard convection, the planetary boundary layer, or the AFB86 flow. Unlike astrophysical applications, we consider the flow without volumetric heat sources. Further differences between our flow and the planetary boundary layer include, for example, the length scales involved, and the absence of a mean shear.

On the other hand, a common mechanism causes turbulent motions in all these flows. This assumes the existence of common fundamental properties, which, indeed, are well known. They are the presence of a well mixed core region, generation of thermal plumes in unstable thermal boundary layers, and development of a large-scale circulation pattern. The purpose of our investigation is to reveal (i) how these family features transform in the particular case of surface-cooling-driven convection in a stratified layer with isothermal bottom, (ii) what are the distinctive properties of the flow.

The method of large-eddy simulations (LES) is applied. We use the scaling version of the dynamic SGS (subgrid-scale) closure proposed by Wong & Lilly (1994). Particular attention is paid to the question of accurate simulation of free-surface and bottom boundary layers and comparison with DNS (direct numerical simulation) data.

The paper is organized as follows. In § 2, we formulate the problem and provide details of the LES approach and the numerical method. The results of LES computations are discussed in § 3. Section 4 includes the comparison between LES and DNS results. Concluding remarks are given in § 5.

2. Numerical model

2.1. *Formulation of the problem*

We consider a flow in a horizontal layer confined between a rigid no-slip bottom at $z = 0$ and stationary free-slip surface at $z = L_z$ (see figure 2). The flow is assumed homogeneous in both horizontal directions so that periodic boundary conditions with the periodicity length scales L_x and L_y can be applied.

The fluid flow is generated through the thermal convection mechanism arising due to the heat exchange (cooling) at the upper surface. In this study, we neglect the effects of wind stress and surface gravity waves.

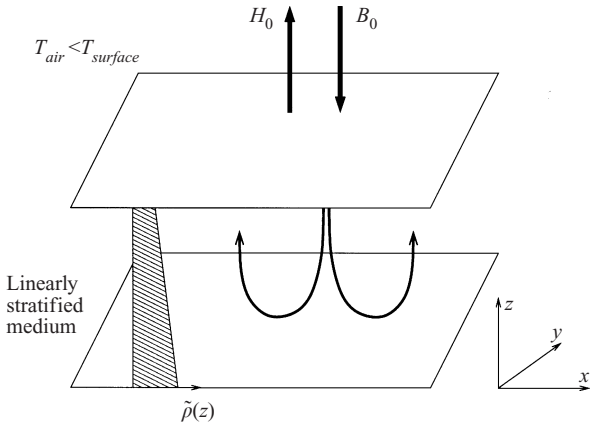

FIGURE 2. Flow geometry; $\tilde{\rho}(z)$ is the initial density distribution, H_0 and B_0 are the heat and buoyancy fluxes at the surface.

In the absence of any motions, the fluid is stably stratified due to the initial temperature and salinity stratification. Adopting the linear approximation, we write the total density field as

$$\rho_{total} = \rho_0 + \frac{\mathrm{d}\tilde{\rho}}{\mathrm{d}z} z + \rho(x, y, z, t), \quad \frac{\mathrm{d}\tilde{\rho}}{\mathrm{d}z} < 0, \tag{1}$$

where ρ_0 and $\mathrm{d}\tilde{\rho}/\mathrm{d}z$ are the reference (bottom) value of the density and a constant vertical density gradient of the quiescent fluid, respectively, and $\rho(x, y, z, t)$ is the density perturbation due to the fluid motion.

Note that we use the traditional Boussinesq decomposition (1) even though there is no mechanism in the system that would support the background stable density gradient $\mathrm{d}\tilde{\rho}/\mathrm{d}z$ after the convective motion sets in. This seems to be a reasonable approach since one of the main goals of our study is to determine the effect (if any) of the initial stratification on the evolution of the turbulent flow.

For constant salinity, temperature and density variations are related as

$$\rho = (-\alpha\rho_0)T, \tag{2}$$

where α is the thermal expansion coefficient.

The flow is described by the standard set of equations based on the Boussinesq approximation

$$\nabla \cdot \boldsymbol{u} = 0, \tag{3}$$

$$\frac{\partial \boldsymbol{u}}{\partial t} + (\boldsymbol{u} \cdot \nabla)\boldsymbol{u} = -\frac{1}{\rho_0}\nabla p - \frac{g}{\rho_0}\boldsymbol{e}_z \rho + \nu \nabla^2 \boldsymbol{u}, \tag{4}$$

$$\frac{\partial \rho}{\partial t} + \boldsymbol{u} \cdot \nabla \rho = -w\frac{\mathrm{d}\tilde{\rho}}{\mathrm{d}z} + \sigma \nabla^2 \rho, \tag{5}$$

where ν is the kinematic viscosity and $\sigma = \kappa/\rho_0 c_p$ is the coefficient of the density (and thermal) diffusion, and $\boldsymbol{e}_z$ is the unit vector in the direction opposing gravity.

The velocity boundary conditions are no slip at the bottom

$$u = v = w = 0 \quad \text{at} \quad z = 0, \tag{6}$$

and the free-slip lid approximation at the top

$$w = \frac{\partial v}{\partial z} = \frac{\partial u}{\partial z} = 0 \quad \text{at} \quad z = L_z. \tag{7}$$

To obtain the density boundary condition at the upper surface, we approximate the cooling process by a constant heat flux H_0 that can be estimated, for example, with Newton's law of cooling $H_0 = h(T_{air} - T_{surface})$. Taking into account (2) and (1) we obtain

$$\left.\frac{\partial \rho}{\partial z}\right|_{z=L_z} = -\frac{\partial \tilde{\rho}}{\partial z} - H_0 \frac{\alpha}{\sigma c_p}. \tag{8}$$

There are two options for the density boundary condition at the bottom. The first is to require that the total density is fixed (isothermal condition), which gives

$$\rho = 0 \quad \text{at} \quad z = 0. \tag{9}$$

The second is the condition of zero density flux (adiabatic condition) corresponding to

$$\frac{\partial \rho}{\partial z} = -\frac{\partial \tilde{\rho}}{\partial z} \quad \text{at} \quad z = 0. \tag{10}$$

In this study, we concentrate on condition (9).

In order to obtain a non-dimensional formulation of the problem we use the depth L_z as the length scale and $(B_0 L_z)^{1/3}$ as the velocity scale. Here

$$B_0 \equiv |H_0| \frac{\alpha g}{\rho_0 c_p} \tag{11}$$

is the buoyancy flux at the surface. In this work, we neglect the temperature dependence of fluid properties so that the coefficient $\alpha g / \rho_0 c_p$ and hence B_0 can be considered constant.

The choice of the velocity scale is dictated by the fact that the turbulent velocity in open oceanic convection scales as

$$u \approx (B_0 L_z)^{1/3}$$

at high Rayleigh numbers (see e.g. Maxworthy 1997). For the time and pressure scales we use $L_z^{2/3} B_0^{-1/3}$ and $B_0^{2/3} L_z^{2/3} \rho_0$, respectively. The density scale is based on the initial background stratification

$$[\rho] = L_z |\mathrm{d}\tilde{\rho}/\mathrm{d}z|. \tag{12}$$

The non-dimensional equations and boundary conditions are (we keep the same symbols for the non-dimensional variables)

$$\nabla \cdot \boldsymbol{u} = 0, \tag{13}$$

$$\frac{\partial \boldsymbol{u}}{\partial t} + (\boldsymbol{u} \cdot \nabla)\boldsymbol{u} = -\nabla p - Ri\, \boldsymbol{e}_z \rho + Re^{-1} \nabla^2 \boldsymbol{u}, \tag{14}$$

$$\frac{\partial \rho}{\partial t} + \boldsymbol{u} \cdot \nabla \rho = w + (Re\, Pr)^{-1} \nabla^2 \rho, \tag{15}$$

$$u = v = w = \rho = 0 \quad \text{at} \quad z = 0, \tag{16}$$

$$w = \frac{\partial v}{\partial z} = \frac{\partial u}{\partial z} = 0 \quad \text{at} \quad z = 1, \tag{17}$$

$$\frac{\partial \rho}{\partial z} = 1 + Re\, Pr\, Ri^{-1} \quad \text{at} \quad z = 1. \tag{18}$$

The variable part of the total density field $\rho_{var} = \rho_{total} - \rho_0$ becomes, in non-dimensional form,

$$\rho_{var} = -z + \rho(x, y, z, t), \tag{19}$$

where $-z$ stands for the non-dimensional initial density distribution.

The non-dimensional parameters are the Reynolds, Prandtl and Richardson numbers given by

$$Re \equiv \frac{L_z^{4/3} B_0^{1/3}}{\nu}, \quad Pr \equiv \frac{\nu}{\sigma}, \quad Ri \equiv (N L_z^{2/3} B_0^{-1/3})^2, \tag{20}$$

where

$$N \equiv (|\mathrm{d}\tilde{\rho}/\mathrm{d}z| g \rho_0^{-1})^{1/2}$$

is the buoyancy frequency. The definition of the Richardson number is different from the more conventional definition $Ri = N^2(\mathrm{d}\tilde{u}/\mathrm{d}z)^{-2}$ that uses the gradient of the mean velocity $\tilde{u}$, which is absent in our simulations.

An alternative to using the Reynolds number is to formulate the problem in terms of the Prandtl number and the flux Rayleigh number

$$Ra \equiv \frac{B_0 L_z^4}{\nu \sigma^2} \tag{21}$$

and to express

$$Re = (Ra\, Pr^{-2})^{1/3} \tag{22}$$

A typical situation considered in the present study is characterized by

$$Re \gg 1, \quad Pr = 1, \quad Ri > 1. \tag{23}$$

2.2. *LES model*

The large-eddy simulation (LES) technique has been increasingly applied in the last three decades to overcome the inherent limitations of direct numerical simulations for flows with low and moderate Reynolds number. In LES, a fine computational grid is used to calculate only the part of the velocity and density fields corresponding to length scales larger than the grid spacing. This resolved part of the flow can be thought of as obtained as the result of spatial filtering or averaging of the actual flow field with the filter width $\bar{\Delta}$ equal to the grid spacing, and is typically denoted using an overbar as $\bar{\boldsymbol{u}}$ or $\bar{\rho}$. The effect of the velocity and density fluctuations at smaller scales is modelled using one of the subgrid-scale (SGS) closure methods.

We apply the scaling version of the dynamic SGS closure proposed for turbulent thermal convection by Wong & Lilly (1994, hereafter referred to as WL94). Since a detailed discussion can be found there, only a brief account is given in this paper.

We start with the classical Smagorinsky model generalized to include buoyancy effects and express the SGS stress tensor

$$\tau_{ij} \equiv \overline{u_i u_j} - \bar{u}_i \bar{u}_j \tag{24}$$

and SGS density flux

$$\tau_{\rho i} \equiv \overline{\rho u_i} - \bar{\rho} \bar{u}_i \tag{25}$$

in terms of the resolved strain tensor

$$\bar{S}_{ij} \equiv \frac{1}{2} \left(\frac{\partial \bar{u}_i}{\partial x_j} + \frac{\partial \bar{u}_j}{\partial x_i} \right)$$

and density gradient $\partial\bar{\rho}/\partial x_i$, respectively:

$$\tau_{ij} - \frac{\delta_{ij}}{3}\tau_{kk} = -2\nu_t \bar{S}_{ij}, \tag{26}$$

$$\tau_{\rho i} = -\kappa_t \frac{\partial \bar{\rho}}{\partial x_i}. \tag{27}$$

To determine the eddy viscosity and diffusivity coefficients ν_t and κ_t we apply the dynamic procedure originally due to Germano *et al.* (1991) and WL94. Simple arguments based on Kolmogorov scaling lead to the assumption that ν_t and κ_t are proportional to $\bar{\Delta}^{4/3}$ with universal coefficients of proportionality (Kolmogorov 1941). These coefficients are estimated through the use of the dynamic procedure. The resolved flow fields are subjected to a second filtering operation with a larger 'test' filter width $\hat{\Delta}$. The test-filtered variables are denoted as $\hat{\bar{\boldsymbol{u}}}$, $\hat{\bar{\rho}}$. Coefficients ν_t and κ_t are then determined using the least-square method:

$$\nu_t = \frac{1}{2}\frac{\sum_{i,j}[(L_{ij} - \delta_{ij}L_{kk}/3)(\hat{\bar{S}}_{ij} - \delta_{ij}\hat{\bar{S}}_{kk}/3)]}{[1 - (\hat{\Delta}/\bar{\Delta})]^{4/3}\sum_{ij}(\hat{\bar{S}}_{ij} - \delta_{ij}\hat{\bar{S}}_{kk}/3)^2]}, \tag{28}$$

$$\kappa_t = \frac{\sum_i R_{\rho i}\partial\hat{\bar{\rho}}/\partial x_i}{[1 - (\hat{\Delta}/\bar{\Delta})]^{4/3}\sum_i(\partial\hat{\bar{\rho}}/\partial x_i)^2} \tag{29}$$

(see WL94 for details). The tensors L_{ij} and $R_{\rho i}$ are calculated using the test-filtered flow fields as

$$L_{ij} = \widehat{\bar{u}_i\bar{u}_j} - \hat{\bar{u}}_i\hat{\bar{u}}_j, \tag{30}$$

$$R_{\rho i} = \widehat{\bar{\rho}\bar{u}_i} - \hat{\bar{\rho}}\hat{\bar{u}}_i. \tag{31}$$

The scaling version of the dynamic model offers three essential advantages over the more traditional version due to Cabot (1992) and Sullivan & Moeng (1992) referred to as the 'stratification formulation' in WL94. First, it results in a considerable reduction of computational time (about 1.7 times according to WL94). Second, the eddy coefficients ν_t and κ_t are calculated independently so that no iterative procedure is necessary. Finally, the scaling formulation allows one to avoid including the physically unjustified buoyancy production term in the constitutive equations for ν_t and κ_t.

A comment is in order regarding the assumed relation (27) between the SGS density flux $\tau_{\rho i}$ and the grid-scale density gradient $\partial\bar{\rho}/\partial x_i$. Some authors (see, for example, Kimmel & Domaradzki 2000) rightly argue that this analogy to the eddy viscosity assumption is rather crude and may be violated locally in real convective flows. This critique, however, was mostly directed towards the classical Smagorinsky method, where ν_t and κ_t are connected by the assumption of constant turbulent Prandtl number. On the contrary, in the method we apply here, ν_t and κ_t are determined independently using the dynamic procedure so that the turbulent Prandtl number does not need to be prescribed. As was shown in WL94 and further discussed in § 4, this method offers important advantages over the Smagorinsky method and is capable of reproducing essential characteristics of the flow.

In the calculations presented in this paper, the width of the test filter is chosen as twice the grid size, $\hat{\Delta} = 2\bar{\Delta}$. The test-filtered quantities are obtained by volume

averaging over the two adjacent grid cells in each horizontal direction. No test filtering is made in the vertical direction, where we use a computational grid which is much finer than the horizontal grid, so that the flow is fully resolved down to the smallest scales. The reason for such an approach is the necessity to resolve the velocity and density boundary layers as discussed below in § 3.1.

Another important difference between our formulation and the scaling formulations used in WL94 is that we do not apply any plane or local volume averaging of the numerator and denominator of the fractions (28) and (29). Such an averaging is typically used with the dynamic model to suppress a numerical instability. We found that the instability can be efficiently prevented by smoothing the calculated ν_t and κ_t fields after each time step with the help of the hyperviscosity compact filter proposed by Lele (1992).

2.3. *Numerical method*

A combination of pseudo-spectral and finite-difference methods is used to calculate the flow. In the horizontal directions, we exploit the advantage of the periodicity and apply the pseudo-spectral technique based on the fast Fourier transform. Spatial derivatives are evaluated using the Fourier representation, while multiplications required for the nonlinear terms are performed in physical space.

In the vertical direction, the computational grid is strongly clustered near the upper and lower boundaries so as to allow proper resolution of density and velocity boundary layers. The physical coordinate z is transformed into the numerical coordinate ζ, where the grid is uniform, according to

$$z = \tfrac{1}{2}[1 + \gamma^{-1} \tanh(a(\zeta - \tfrac{1}{2}))], \quad z \in [0,1], \quad \zeta \in [0,1], \quad \gamma = \tanh\frac{a}{2}. \tag{32}$$

The degree of clustering is determined by the positive parameter a. A typical value used in the calculations was $a = 3.5$.

The equations are discretized in the transformed variable ζ using the staggered central-difference scheme of second order. Integer points $\zeta_i = i\Delta\zeta$, $i = 0, \ldots, N_z$, are used to calculate velocity and density perturbations and satisfy the momentum and density equations. The pressure field and incompressibility condition are treated at the half-integer points $\zeta_{i+1/2} = (i + 1/2)\Delta\zeta$.

For the time-differencing, we use a fully explicit implementation of the time-splitting (also called the projection or fractional step) method based on the third-order Adams–Bashforth scheme. To achieve greater numerical efficiency, the scheme was modified to permit variable time-step changes according to a temporal stability criteria (see Slinn & Riley 1998 for more details).

The Poisson equation for the pressure arising in connection with the time-splitting method is solved using the pseudo-spectral technique in the periodic directions and inverting a tri-diagonal matrix in the vertical direction. The boundary conditions for the pressure are generated by projecting the momentum equations onto the normals to the bottom and free surface.

To verify the code, we performed several DNS simulations in a smaller domain and carefully examined the initial instability of the surface conductive layer (more details on the DNS runs are in § 4). It was found that both the critical Rayleigh number and the wavenumber of the most unstable mode are in agreement with the linear stability theory (see Maxworthy 1997 and references therein). Further verification was delivered by the fact that, as discussed in § 3.2, the energy conservation principle was satisfied with acceptable accuracy by the calculated solutions.

3. Numerical experiments

3.1. *Parameters and numerical resolution*

The results of two full-scale numerical experiments are discussed in this section (additional computations performed to validate the model against DNS results are presented in § 4). In both experiments, the horizontal dimensions L_x and L_y are six times larger than the depth L_z, the Reynolds number (20) is $Re = 1200$, and the molecular Prandtl number is $Pr = 1$. The corresponding flux Rayleigh number (21) is 1.728×10^9. The only difference between the two experiments is in the value of the bulk Richardson number considered, $Ri = 2$ in the first experiment and $Ri = 10$ in the second. The numerical resolution is based on 128 Fourier collocation points in each of the horizontal directions and 150 discretization points in the vertical direction.

Later in this subsection, we will discuss the reasons that determined our choice of flow parameters and resolution. The discussion will appeal to existing numerical simulations of turbulent convection such as works by Grötzbach (1983), Eidson (1985), Kerr (1996), and Kimmel & Domaradzki (2000).

The requirements for an adequate numerical (DNS) simulation of turbulent convection in horizontal layers were originally formulated and verified by Grötzbach (1983). First, the horizontal dimensions of the computational domain should be large enough to minimize the influence of periodic boundaries on the large-scale flow structures. Second, the computational grid should be fine enough to resolve the smallest-scale turbulent motions. Finally, the vertical grid width near the boundaries should provide an adequate resolution of thin velocity and density (temperature) boundary layers.

It has been demonstrated in the simulations mentioned above that $L_x = L_y \geqslant 6L_z$ usually suffices to minimize the impact of periodic boundaries on the large-scale structures. Cells with aspect ratio between 6 and 10 are typically used in experiments (see e.g. AFB86). Our calculations confirm that the computational domain with $L_x/L_z = L_y/L_z = 6$ provides enough space for establishing a large-scale circulation pattern, even though, as discussed below, the specific spatial features of the circulation are, probably, influenced by periodic boundary conditions.

The second requirement is satisfied by our vertical grid and is accounted for in the x- and y-directions through application of a SGS model. However, the resolution should be kept fine enough to sufficiently resolve single large-scale thermal plumes developing in the turbulent flow. The comparison between DNS and LES results in § 4 shows that this requirement is fulfilled in our simulations.

The third requirement still presents a serious problem in LES of turbulent convection. There are three different boundary layers in the flow considered in this paper: the velocity boundary layer at the bottom and the density (thermal) boundary layers at the bottom and at the upper surface. Obviously, an adequate description of the flow can be achieved only if the impact of boundary layers on the core flow is properly accounted for.

Any attempt to apply the SGS model in the vertical direction would, thus, require a DNS-like resolution of the boundary layers (Eidson 1985) or wall corrections. Unfortunately, the widely used wall corrections cannot be justifiably applied to our problem. The wall function models developed and verified for channel flow (see e.g. Schumann 1975) have to be excluded because they assume the existence of a persistent mean velocity near the bottom and are designed specifically for high Reynolds number flows over rough surfaces. Neither of these conditions is fulfilled in our flow. Another approach based on the Monin–Obukhov relation was developed using the measurements made in the convective planetary boundary layer (see e.g.

Schmidt & Schumann 1989). This method cannot be applied to our flow for the same reasons as the channel flow models and because of other differences between the conditions in the planetary boundary layer and those in an oceanic water column.

Our preliminary attempts to model the surface heat flux using a bulk parameterization into an unresolved thermal boundary layer (see e.g. Denbo & Skyllingstad 1996) produced flow features similar in behaviour and resulting net fluxes to the resolved boundary layer simulations. No satisfactory treatment could, however, be found for the unresolved no-slip boundary conditions at the sea floor.

In this paper, our main aim is to achieve a better understanding of the basic properties of the flow induced specifically by surface cooling. Therefore, we avoid uncertainties introduced by wall models and apply the method of complete numerical resolution of the vertical flow structure including the velocity and density boundary layers. An inevitable price to be paid for that is a moderate value of the Reynolds number that is about two orders of magnitude smaller than the Reynolds number in real oceanic flows.

The following estimate can be given for the Reynolds and Richardson numbers during actual adverse weather events in the ocean. The estimate is based on CTD (conductivity, temperature and depth) casts from a ship (Dhanak, unpublished). The measurements were made in littoral waters off the coast of Florida during winter time. We use the value $5.3 \times 10^{-10}\,\mathrm{m^2\,kg^{-1}}$ for the constant $\alpha g/c_p\rho_0$, which approximately corresponds to water temperature in the range 20 °C to 25 °C studied here. Considering a typical situation with the surface heat flux $H_0 \approx 200\,\mathrm{W\,m^{-2}}$ and the initial density gradient $\mathrm{d}\tilde{\rho}/\mathrm{d}z \approx 0.02\,\mathrm{kg\,m^{-4}}$, a flow in a layer, which is 10 m deep, would have $Re \approx 10^5$ and $Ri = 200$. Our simulations with $Re = 1200$ and $Ri = 2$ can be thought as of, for example, carried out with the same background density gradient, and with $L_z = 0.34\,\mathrm{m}$ and $H_0 = 212\,\mathrm{W\,m^{-2}}$ (for $Ri = 2$). The flow with $Re = 1200$ and $Ri = 10$ could have the same L_z and H_0 and five times larger density gradient, or the same $\mathrm{d}\tilde{\rho}/\mathrm{d}z$ and $L_z = 0.51\,\mathrm{m}$ and $H_0 = 42\,\mathrm{W\,m^{-2}}$.

We would like to make a comment regarding the duration of our numerical experiments and its relation to the duration of an actual adverse weather event. If we assume (not having any strong reason for that) that the flow evolution described by the non-dimensional curves in figures 3 and 4 could be extrapolated to the case of $H_0 \approx 200\,\mathrm{W\,m^{-2}}$ and $L_z = 10\,\mathrm{m}$ then the total dimensional duration of each run would be about 25 hours, which seems sufficient to capture the principal features of the flow.

3.2. *Flow evolution*

The flow evolution is illustrated in figure 3, which shows volume-averaged kinetic and potential energies

$$KE_{xy} = \tfrac{1}{2}\langle u^2 + v^2\rangle_v, \quad KE_z = \tfrac{1}{2}\langle w^2\rangle_v, \quad PE = \tfrac{1}{2}Ri\langle\rho^2\rangle_v \tag{33}$$

as functions of time. The brackets $\langle\ldots\rangle_v$ are used hereafter for volume averaging, while the same brackets without subindex $\langle\ldots\rangle$ are reserved for the averaging over a horizontal plane.

In both experiments, the heat flux is abruptly applied at $t = 0$ to the upper surface of the flow consisting of the background density distribution and infinitesimal velocity perturbations. Initially, only the potential energy grows, which corresponds to the growth of the conductive boundary layer at the upper surface. In a short period of time, cold heavy fluid diffuses deep enough so that the Rayleigh number based on the depth of the conductive layer exceeds the critical stability value of about

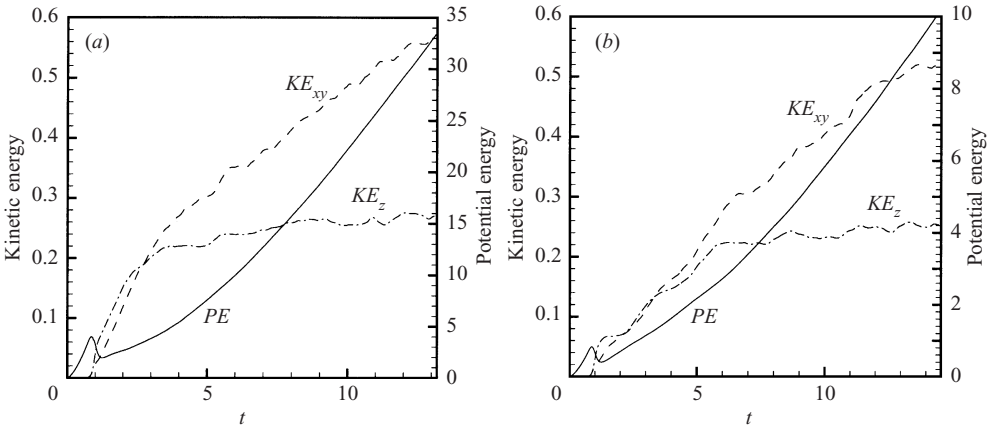

FIGURE 3. Volume-averaged kinetic and potential energies (33) as functions of time. (*a*) calculations with $Ri = 2$; (*b*) calculations with $Ri = 10$.

5×10^3 (Maxworthy 1997). The conductive layer becomes unstable and gives rise to a convective flow in the form of multiple descending plumes. The beginning of plume generation coincides with the drop of potential energy and the start of the growth of the kinetic energy curves in figure 3.

The subsequent flow evolution can be divided into two stages. During the first stage, the plumes move downward, interacting with one another and generating turbulent motions. Typical characteristics of this stage are rapid growth of both the vertical and horizontal components of the kinetic energy and increasing slope of the potential energy curve.

The second stage, which can be considered as that of fully developed turbulence, is characterized by a plateau in the vertical kinetic energy curve, slightly reduced growth of the horizontal kinetic energy, and the slope of the potential energy curve approaching a constant.

It should be stressed that the flow we consider in this study is unsteady even in the statistical sense. Unlike, for example, Rayleigh–Bénard convection, where, in a developed state, the energy input through one surface is balanced by the output through the other surface, the total energy in our system grows during the entire numerical experiment. Clearly, this happens because the heat flux through the isothermal bottom is not equal to the imposed surface heat flux.

The unsteadiness of the flow resembles the behaviour of turbulent thermal convection between heated and thermally insulated surfaces (see AFB86). It can be proven that, in the latter, the horizontally averaged temperature of the entire layer increases linearly with time. We examined the time evolution of a horizontally averaged density profile in our simulations and found that it moved as a whole towards larger density perturbations. The differences $\langle \rho(z) - \rho(0) \rangle$ experienced continuous, though irregular, growth. More detailed discussion of the time evolution of the flow is pursued in § 5.

One has to guard against too close an analogy between our system and the system studied in AFB86. In our case, the isothermal boundary condition will, eventually, lead to establishing a statistically steady state, in which the temperature difference between the cold core and the bottom will grow strong enough to produce the heat flux that will balance the surface heat flux. There are several reasons why we study the initial unsteady phase of the flow and do not pursue the final steady state. First, according

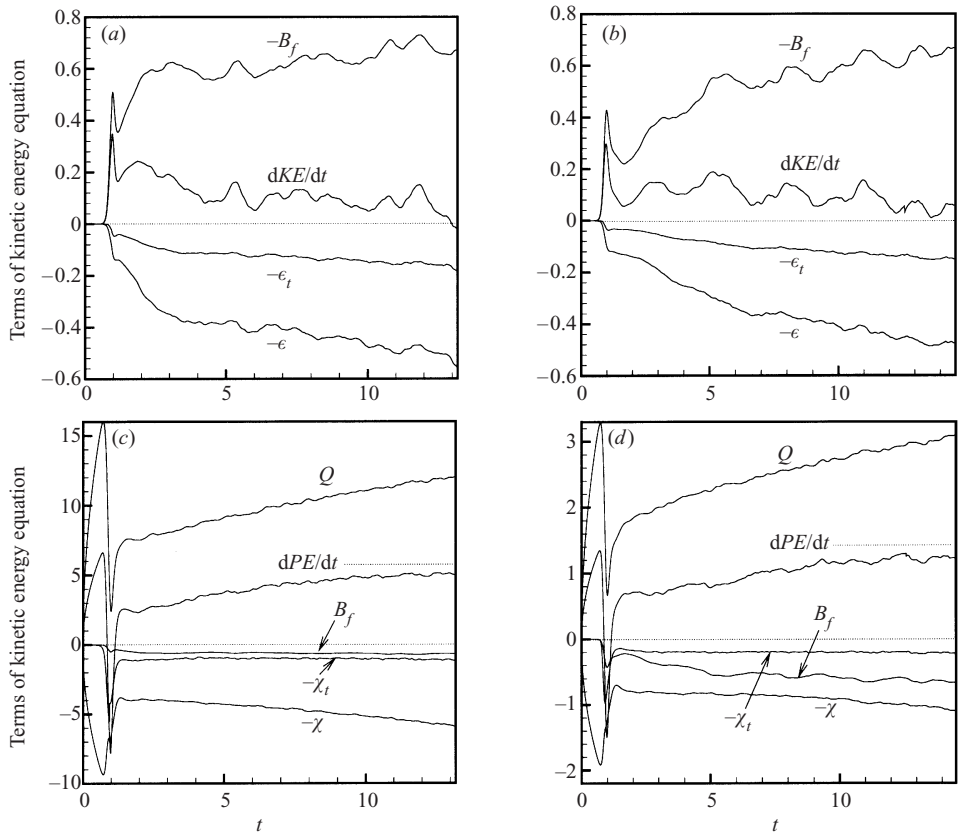

FIGURE 4. Terms of the kinetic (a, b) and potential (c, d) energy equations (34) and (35) as functions of time. Plots (a) and (c) are for the run with $Ri = 2$, and plots (b) and (d) are for the run with $Ri = 10$. Horizontal dotted lines are to show the zero level and to demonstrate the deviation of the slope of potential energy curves from a constant.

to the estimates made in the end of § 3.1, the total duration of our experiments corresponds to the typical time scale of the ocean phenomenon under consideration. Furthermore, the isothermal idealization of the bottom boundary condition becomes less justified at the larger temperature drop across the bottom boundary layer achieved at the steady state.

Figure 4 illustrates the energy balance in the flow. The energy equations are

$$\frac{\mathrm{d}}{\mathrm{d}t}KE = -\epsilon - \epsilon_t - B_f, \tag{34}$$

$$\frac{\mathrm{d}}{\mathrm{d}t}PE = -\chi - \chi_t + B_f + Q, \tag{35}$$

where $KE = KE_{xy} + KE_z$ and PE are volume-averaged kinetic and potential energies,

$$\epsilon = \frac{2}{Re}\langle S_{ij}^2 \rangle_v \quad \text{and} \quad \epsilon_t = 2\langle \nu_t S_{ij}^2 \rangle_v \tag{36}$$

are resolved and SGS rates of dissipation of kinetic energy,

$$\chi = \frac{Ri}{Pr\,Re}\langle (\nabla\rho)^2 \rangle_v \quad \text{and} \quad \chi_t = Ri\langle \kappa_t (\nabla\rho)^2 \rangle_v \tag{37}$$

are resolved and SGS rates of dissipation of potential energy,

$$Q = \frac{Ri}{Pr\,Re}\left\langle \rho \frac{\partial \rho}{\partial z}\bigg|_{z=1} \right\rangle \tag{38}$$

is the horizontally averaged potential energy flux at the upper surface, and

$$B_f = Ri\langle w\rho \rangle_v \tag{39}$$

is the buoyancy flux.

It can be seen in figures 4(*c*) and 4(*d*) that the growth rate of potential energy changes very slowly in the developed turbulent flow so that it can be considered approximately constant. It is also interesting that ϵ_t and χ_t are considerably smaller than, correspondingly, ϵ and χ, implying that the modelled fluctuations at subgrid scales are responsible for only a fraction of the total dissipation of kinetic and potential energies. However, as will be discussed later in this section, the major portion of the dissipation at resolved scales occurs near the upper and lower boundaries. In the core flow, ϵ_t is comparable to ϵ, and χ_t is approximately equal to χ.

The energy balance (34) and (35) was accurately reproduced by the numerical model. The difference between the left- and right-hand sides was found to remain within 2% of $\mathrm{d}KE/\mathrm{d}t$ and $\mathrm{d}PE/\mathrm{d}t$, respectively.

3.3. *Spatial structure of the flow*

The spatial structure of the flow at different stages of its evolution is illustrated in figure 5. It has to be stressed that the horizontal numerical resolution is not sufficient to resolve the finest features of flow patterns, which are averaged out by the filtering procedure. However, as discussed in more detail in § 4, the LES simulations adequately describe the most important features of the flow dynamics.

Figure 5 shows the distribution of the variable part of the total density field $\rho - z$ in the vertical cross-section taken at $y = L_y/2$. Here, ρ is the density perturbations, and $-z$ stands for the non-dimensional background stratification. The constant reference density ρ_0 is not included.

Two snapshots are shown for each numerical experiment. The flow during the initial developing phase shown in figures 5(*a*) and 5(*c*) is dominated by cold plumes generated at the upper surface and descending toward the bottom. The plume propagation is opposed by the stable background stratification, whose influence is stronger in the case of larger Richardson number (cf. figures 5*c* and 5*a*). This effect is responsible for the considerably longer period of initial flow development observed in the experiment with $Ri = 10$ than in the case with $Ri = 2$ (cf. figures 3*a* and 3*b*).

The flow evolution during the initial phase is similar to the evolution observed in deep ocean convection (for a review see e.g. Maxworthy 1997 or Marshall & Schott 1999).

Typical flow patterns in the developed turbulent state are illustrated in figures 5(*b*) and 5(*d*). Again, the flow is dominated by descending plumes but their number is considerably smaller than during the initial phase. Apart from the areas of strongest plumes, the density field is rather homogeneous in the core flow.

To illustrate the velocity field associated with the descending plumes in fully developed turbulent flow, a part of the vertical cross-section from figure 5(*b*) is shown in figure 6(*a*) with the projections of the velocity vectors plotted upon the density field. One can clearly see strong surface currents directed toward the spot where the plume is generated. Another remarkable feature observed earlier in Rayleigh–Bénard

convection is the bottom velocity boundary layers generated when plumes hit the bottom and spread out.

To quantify the presence of large-scale coherent structures in the flow we calculated two-point velocity correlations over the distances $L_x/2$ and $L_y/2$ in the horizontal directions:

$$C_{xi} = \frac{\langle u_i(\boldsymbol{x},t)u_i(\boldsymbol{x}+0.5L_x\boldsymbol{e_x})\rangle_v}{\langle u_i^2\rangle}, \quad C_{yi} = \frac{\langle u_i(\boldsymbol{x},t)u_i(\boldsymbol{x}+0.5L_y\boldsymbol{e_y})\rangle_v}{\langle u_i^2\rangle}, \tag{40}$$

where u_i, $i = 1, 2, 3$, stand for the velocity components u, v and w, and $\langle\ldots\rangle_v$ is the volume average. The results are shown in figure 7. It can be seen that the transition to developed turbulence is associated with the strong growth of the magnitude of correlation coefficients (40).

The global pattern of the large-scale circulation is presented in figures 6(b) and 8. We show the flow calculated in the run with $Ri = 2$ for the same instant of time as in figures 5(b) and 6(a).

In figure 8, density and vertical velocity fields are plotted in the horizontal cross-sections lying just below the upper surface at $z = 0.994L_z$, at the mid-plane $z = L_z/2$, and at the plane $z = 0.006L_z$ near the lower boundary. The density distribution under the upper surface (figure 8a) is similar to the distributions observed in other convective flows with a free surface, such as convection driven by surface evaporation (Saylor, Smith & Flack 2000) or the solar convection zone (solar granulation, see e.g. Brummel *et al.* 1995). The areas of cold heavy fluid are aligned into large-scale stripes that extend across the entire flow domain.

It can be seen in figures 8(a) and 8(d) that the plume formation starts with cold liquid sheets (blue stripes in figure 8d) leaving the conductive boundary layer at the upper surface. As they descend, the sheets are diffused by turbulent motions and coalesce into broad plumes (see figures 8b and 8e). These structures can be observed down to the bottom boundary layer, where they disappear, losing momentum to the shear flow (see figures 8c and 8f).

An interesting observation can be made regarding the statistical properties of our system with respect to the mid-plane. Different types of horizontal convective layers can be distinguished by such properties. For example, the Rayleigh–Bénard system is statistically symmetric, which can be seen, for example, in the distinctive symmetry or anti-symmetry of horizontally averaged vertical profiles. The reason for that is, of course, the symmetry of upward and downward flows. The upward motion of hot fluid occurs in the same manner as the downward motion of the cold fluid. On the contrary, the system with heated bottom and insulated top studied in AFB86 is completely asymmetric. The thermal plumes are generated at the bottom surface only.

Our system can be considered as occupying an intermediate position between the two mentioned above. The flow is strongly asymmetric during the initial stages of its evolution. At the later stages, the isothermal bottom becomes considerably warmer than the mixed fluid in the core region. As a result, ascending liquid sheets and plumes develop, similar to those in Rayleigh–Bénard flow. It must be stressed, however, that the ascending sheets and plumes are less pronounced and are characterized by smaller amplitudes of local peaks of velocity and density fluctuations than the descending ones. This conclusion is not apparent on comparison of the corresponding patterns in figure 8. However, as discussed below, it is strongly supported by the skewness profiles and probability density functions (p.d.f.s) of density and vertical velocity fluctuations. Another manifestation of the asymmetry is that the surface currents replace the shear flow as a sink of momentum of plumes approaching the upper surface.

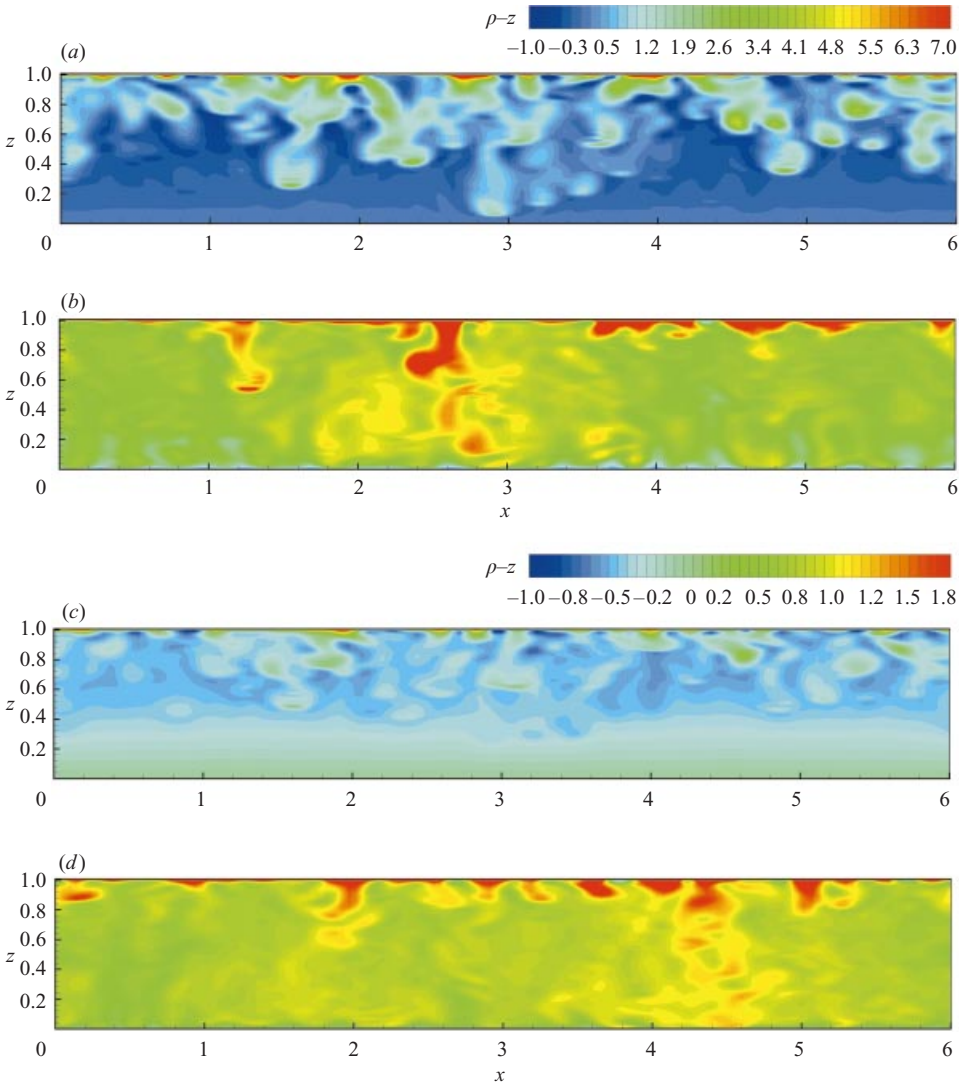

FIGURE 5. Non-dimensional density distributions in the vertical cross-section at $y = L_y/2$. Typical flow patterns during initial $t = 1.81$ (a, c) and developed $t = 11.52$ (b, d) stages are shown for both experiments; (a, b) $Ri = 2$, (c, d) $Ri = 100$.

A remarkable feature of the flow that can be seen in figure 8 is that the upward and downward motions are organized into a large-scale pattern with the upward flow areas (red and yellow colours in figure 8*e*) located between the broad bands of downward flow (blue and deep green colours in figure 8*e*). For further illustration of this phenomenon two density isosurfaces are plotted in figure 6(*b*). The isosurface with $\rho = 7$ (red) is thought to be associated with the outer boundary of descending plumes, while the isosurface with $\rho = 3$ (blue) shows the warm liquid sheets ascending from the bottom.

This large-scale pattern is similar to the diagonal pattern detected in the DNS of turbulent Rayleigh–Bénard convection (Kerr 1996). The difference between the diagonal and our somewhat distorted shape can be attributed to the asymmetry

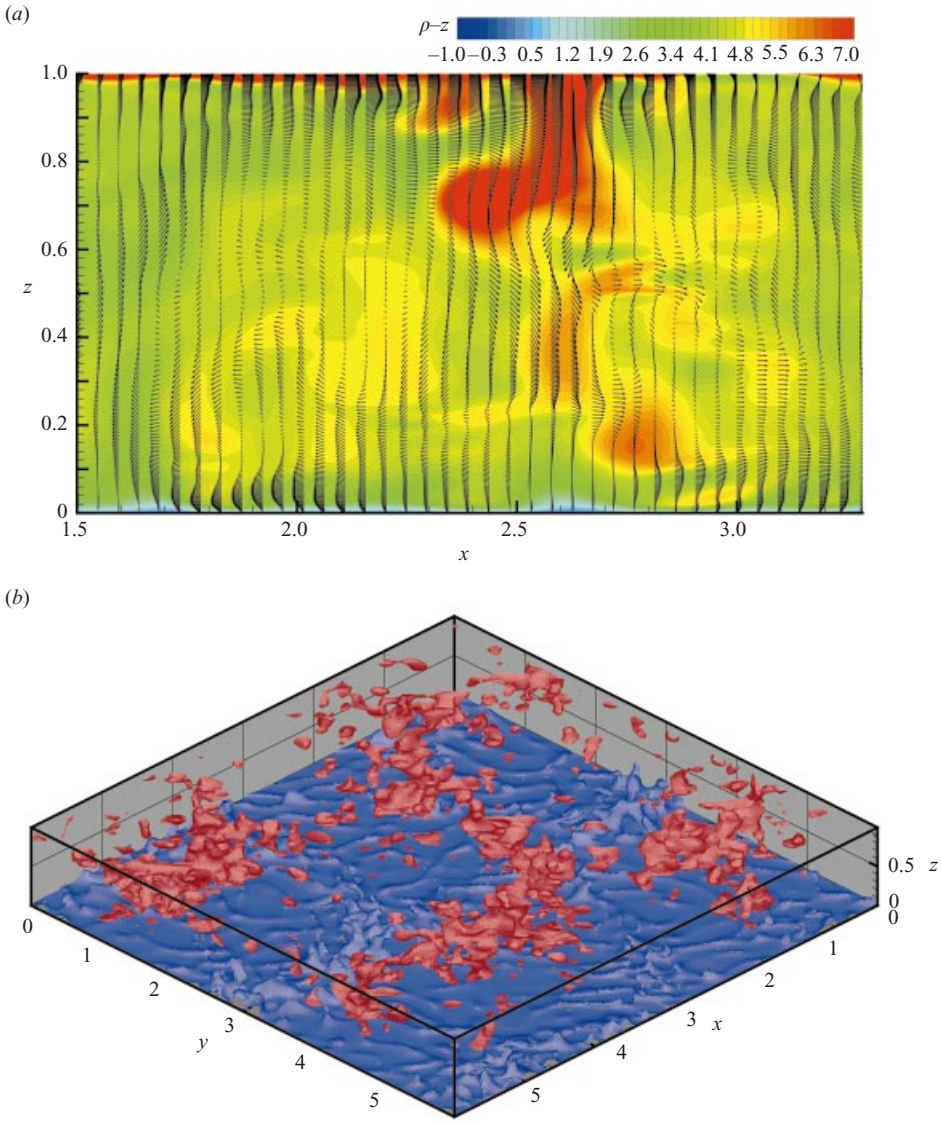

FIGURE 6. (*a*) Flow calculated with $Ri = 2$ at $t = 11.52$. A part of the vertical cross-section in figure 5(*b*) is reproduced with projections (u, w) of the velocity vectors plotted upon the density distribution. (*b*) Three dimensional plot of two density isosurfaces: $\rho = 7$ (red) and $\rho = 3$ (blue). The upper part of the $\rho = 7$ isosurface is removed to make the interior visible.

between the upward and downward flows in our problem. It should be stressed, however, that both our pattern and the diagonal pattern obtained by Kerr are affected by the periodic boundary conditions.

The impact of the boundary conditions can be estimated from the data presented in figure 7. In principle, the correlations (40) should vanish to ensure an adequate representation of the dynamics of large-scale structures (see Moin & Mahesh 1998 for a discussion). Figure 7 shows that as the developing large-scale circulation pattern grows, it becomes affected by periodic boundaries. This effect is rather involved and will be a subject of future investigations. For now, we may state that the development of large-scale structures has been proven by the simulations, although

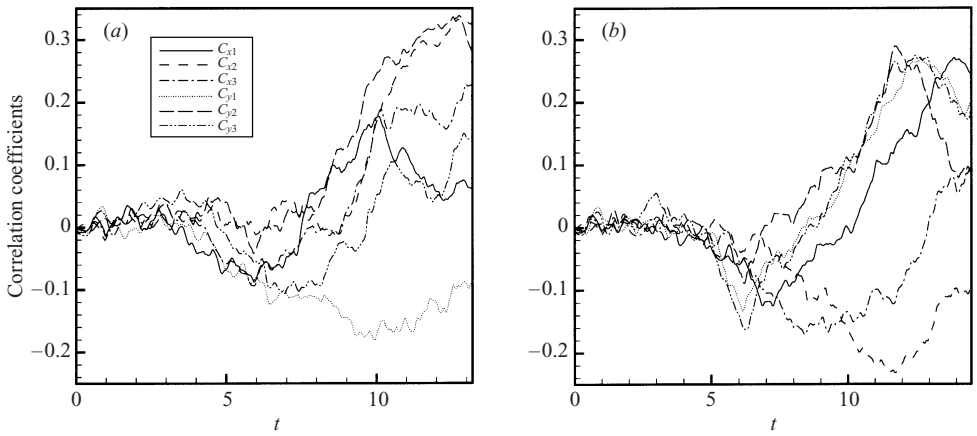

FIGURE 7. Correlation coefficients (40) calculated in the runs with $Ri = 2$ (a) and with $Ri = 10$ (b).

the exact details of these structures should not be considered to be generally valid. A similar situation was met in the studies of Rayleigh–Bénard convection. Global circulation patterns were detected in simulations by Kerr (1996) and in large aspect ratio experiments by Krishnamurti & Howard (1981). The difference between the numerical and experimental results was that a much more regular structure, clearly affected by the periodicity, was observed in the simulations.

Finally, we would like to discuss the question of the possibility of a large-scale flow associated with slow horizontal drift of the plumes. Such a flow was earlier detected by Krishnamurti & Howard (1981) and in low Prandtl number experiments by Cioni, Ciliberto & Sommeria (1997). In an attempt to detect similar drifting flow we visualized velocity and density fields in horizontal and vertical cross-sections. No noticeable drift was observed on the time scale of our numerical experiment; the plume generation happened at approximately the same locations during the entire period of developed turbulence. This observation, of course, does not exclude the possibility of drifting flow at larger time scale or in a cell with larger aspect ratio. We note further that, in our preliminary two-dimensional DNS of the convection problem, vertically varying horizontal drift was produced.

3.4. *Vertical profiles and distribution functions*

Vertical profiles of horizontally and time-averaged flow properties are presented in figures 9–11. The time averaging is performed during the phase of developed turbulent flow over the period $8.33 < t < 13.17$ in the run with $Ri = 2$, and over the period $9.22 < t < 14.55$ at $Ri = 10$. Different intervals are used for time averaging because stronger stratification at $Ri = 10$ leads to a longer stage of initial development of the flow and, thus, to a shift of the interval of developed turbulence towards larger t.

As we have already discussed in § 3.2, the flow considered in this paper is statistically unsteady. The most prominent manifestation of the unsteadiness is the strong continuous growth of density perturbations (see curves of potential energy in figure 3) associated with the continuous cooling of the entire domain. Therefore, for time averaging of flow properties associated with the density field we used profiles calculated as $\langle f \rangle / \langle f \rangle_v$, i.e. horizontally averaged vertical profiles normalized by the volume average calculated for the same t. The changes in the amplitude of velocity fluctuations are much slower. Accordingly, a standard time averaging procedure was used for all quantities that do not involve density.

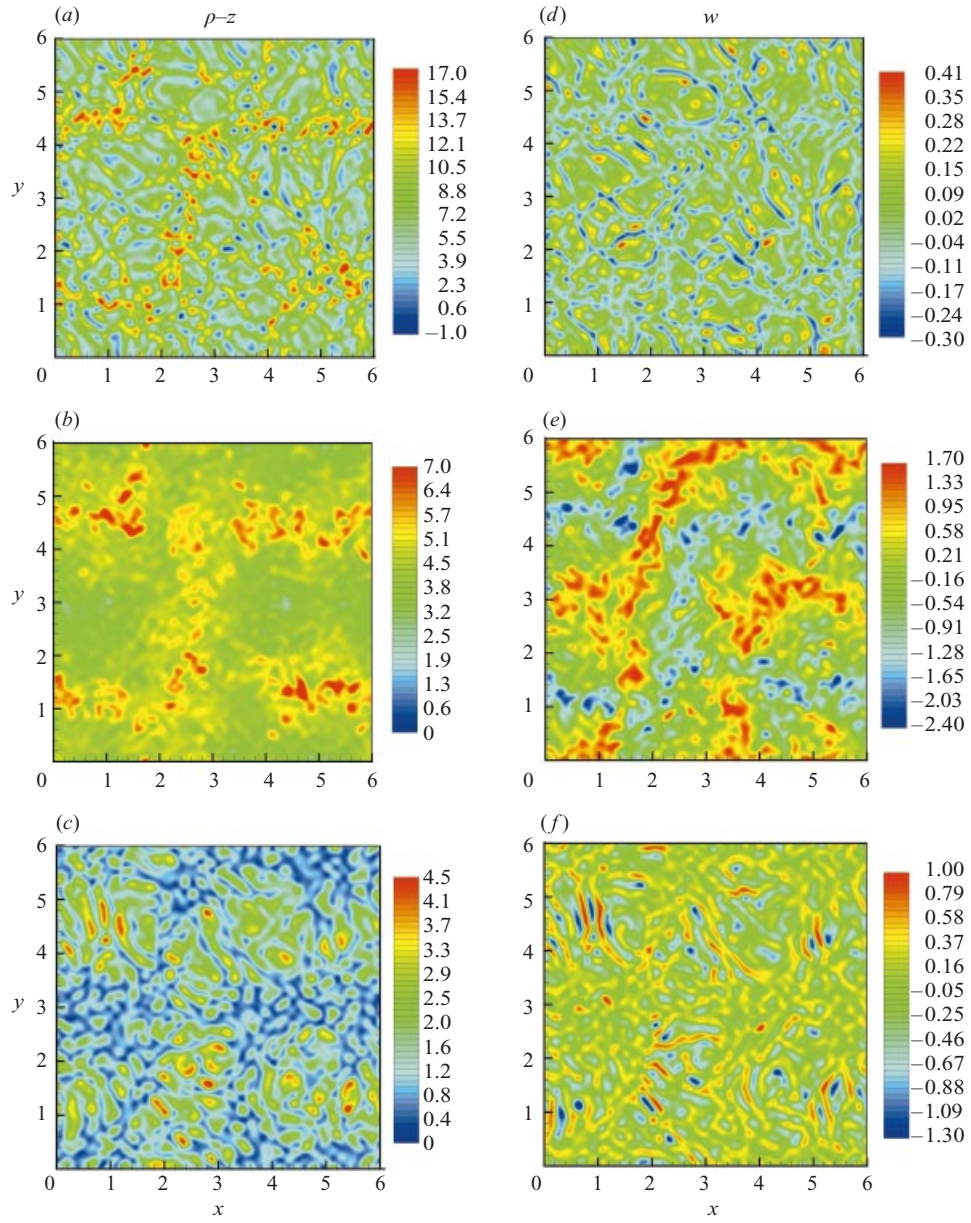

FIGURE 8. Structure of the flow calculated at $t = 11.52$ in the run with $Ri = 2$. Density perturbations ρ (a, b, c), and vertical velocity w (d, e, f) are shown in horizontal cross-sections at $z = 0.994L_z$ (a, d), $z = L_z/2$ (b, e), and $z = 0.006L_z$ (c, f). Upper limits of contour distributions for density, and both upper and lower limits for velocity are taken at 85% of the maximum or minimum values, respectively.

The following discussion intensively uses comparison between our results and the results obtained for two similar systems: Rayleigh–Bénard flow (see e.g. Deardorff & Willis 1967 and Kerr 1996) and the flow between heated bottom and insulated top rigid plates studied in AFB86. In order not to overload the discussion we avoid comparison with other members of the same family such as, for example, the planetary boundary layer.

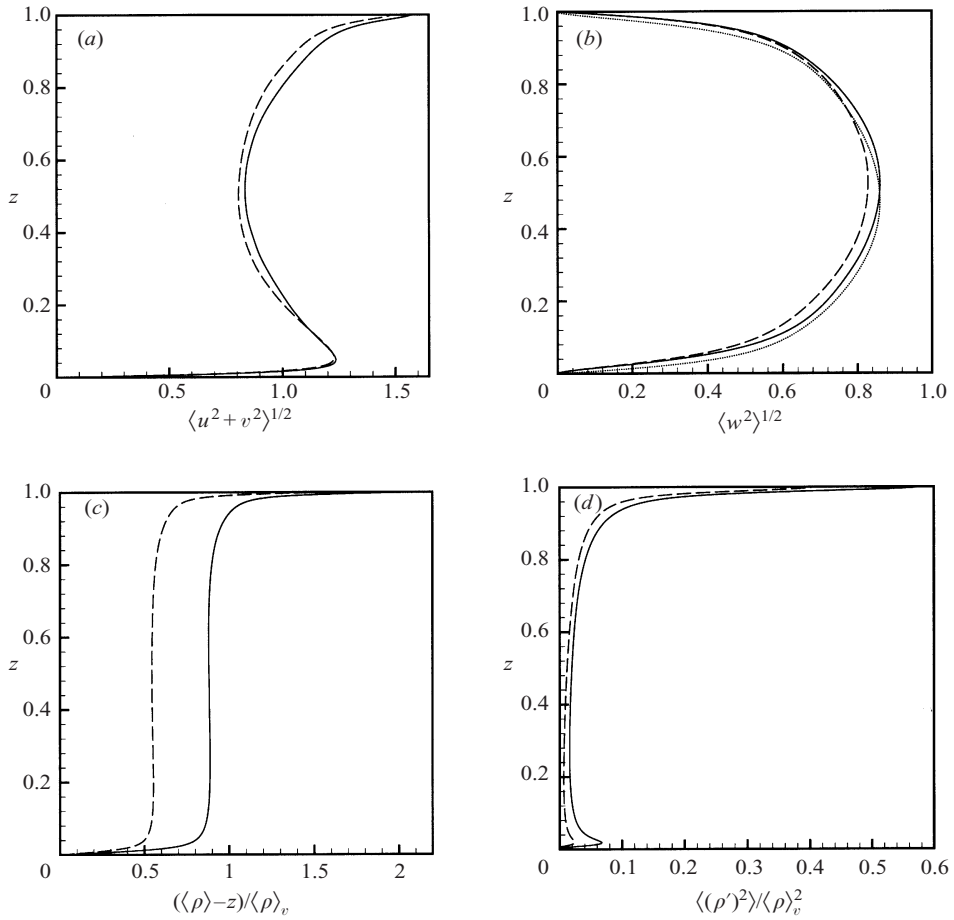

FIGURE 9. Time-averaged profiles of r.m.s. horizontal velocity (*a*), r.m.s. vertical velocity (*b*), variable part of normalized total density (*c*), and normalized density variance (*d*). For normalization in (*c*) and (*d*), volume-averaged density perturbation $\langle\rho\rangle_v$ is used. ———, Calculations with $Ri = 2$; – – –, calculations with $Ri = 10$. Dotted curve in (*b*) is obtained by symmetric reflection of the solid curve.

Figure 9 presents the profiles of resolved velocity and density fields. The shape of the root-mean-square horizontal velocity profile in figure 9(*a*) demonstrates the most important effect of asymmetry of the boundary conditions at the lower and upper surfaces. Near the bottom, a shear boundary layer is clearly seen, which is, of course, the product of the thermal plumes hitting the wall in exactly the same way as in the Rayleigh–Bénard or AFB86 systems.

Close to the upper surface, the behaviour is completely different. The horizontal velocity grows gradually and reaches its maximum at the surface, thus demonstrating the presence of strong surface currents. The driving mechanisms of these currents are the buoyancy forces associated with the formation of descending plumes and, to smaller degree, the momentum transfer by the ascending plumes.

The profiles of vertical velocity in figure 9(*b*) are very similar to the corresponding profiles in the Rayleigh–Bénard and AFB86 systems. The energy of vertical motion increases toward the middle of the layer. The difference between the three systems is in the symmetry properties with respect to the mid-plane. In Rayleigh–Bénard flow, where the ascending and descending plumes are statistically equally strong, the profile

of $\langle w^2\rangle^{1/2}$ is symmetric. In the system considered in AFB86, no plumes are generated at the insulated surface. Therefore, a strong asymmetry is observed.

It can be seen in figure 9(b) that, in our flow, a combination of stronger descending and weaker ascending plume patterns leads to a slightly asymmetric profile. Comparison between $\langle w^2\rangle^{1/2}(z)$ (solid line) and $\langle w^2\rangle^{1/2}(1-z)$ (dotted line) shows that the root-mean-square vertical velocity in the upper half of the convective layer is slightly larger than in the lower part.

A remarkable feature of the curves in figures 9(a) and 9(b) is that there is nearly no difference between the velocity profiles calculated with $Ri = 2$ and $Ri = 10$. The two numerical experiments can be thought as of performed with the same layer depth and surface buoyancy flux but with different initial density gradients $\mathrm{d}\tilde{\rho}/\mathrm{d}z$. Since the velocity scale used for non-dimensionalization does not include $\mathrm{d}\tilde{\rho}/\mathrm{d}z$ we may conclude that, as expected, the turbulent velocity field in the developed turbulent state is not affected by the initial background stratification.

In agreement with the traditional picture of a well-mixed layer in developed turbulent convection, the horizontally averaged density profile consists of a nearly constant part in the core region and density boundary layers near the upper and lower boundaries. Visualizations showed that neither the slope of $\langle\rho - z\rangle$ in the core flow nor the thickness of the boundary layers change with time. Note that, according to the decomposition (19), the variable part of the total density field is presented by $\rho - z$ and not just by ρ.

The profile of horizontally averaged density variance $\langle(\rho')^2\rangle \equiv \langle(\rho - \langle\rho\rangle)^2\rangle$ is shown in figure 9(d). The lower part of the profile is similar to the corresponding parts observed in Rayleigh–Bénard and AFB86 systems. The variance is approximately constant in the core flow and has a peak near the bottom. On the other hand, the upper parts of the profiles are totally different in all three cases. In Rayleigh–Bénard flow, the lower and upper parts are symmetric. In the AFB86 experiments, the intensity of density fluctuations near the insulated boundary remains at the same level as in the core flow. In our simulations, the profile in figure 9(d) demonstrates that the density fluctuations in the upper boundary layer are much stronger than in the rest of the flow. In particular, averaged density variance at $z = L_z$ is more than tenfold the variance in the core flow. Another illustration of this fact is depicted in figure 8(a–c). One can see that, in comparison with the mid-plane and bottom areas, the density distribution near the top contains much more intense small-scale fluctuations (highly intermittent red and blue spots in figure 8a).

A remarkable property of the flow can be seen in figure 10(a). The horizontally averaged convective buoyancy flux $\langle\rho w\rangle$ is not constant across the core region, as is the case in turbulent Rayleigh–Bénard convection, but a linear function of z. Similar results were obtained in other unsteady systems such as the AFB86 experiments or deep ocean convection (see e.g. numerical simulations of Denbo & Skyllingstad 1996). A constant but non-zero slope of the profile $\langle\rho w\rangle$ is in obvious agreement with the non-steadiness of the flow and with the fact that the slope of $\langle\rho\rangle$ remains constant across the interior of the domain. Indeed, horizontal averaging of all terms in the density equation (15) gives

$$\frac{\partial}{\partial t}\langle\rho\rangle = -\frac{\partial}{\partial z}\langle\rho w\rangle + \frac{1}{Re\,Pr}\frac{\partial^2}{\partial z^2}\langle\rho\rangle. \tag{41}$$

Neglecting the diffusive flux and assuming that $\partial\langle\rho\rangle/\partial t$ is positive and z-independent we come to the necessity of a negative z-independent $\partial\langle\rho w\rangle/\partial z$.

Figures 10(b), 10(c) and 10(d) show, respectively, profiles of eddy viscosity $\langle\nu_t\rangle$,

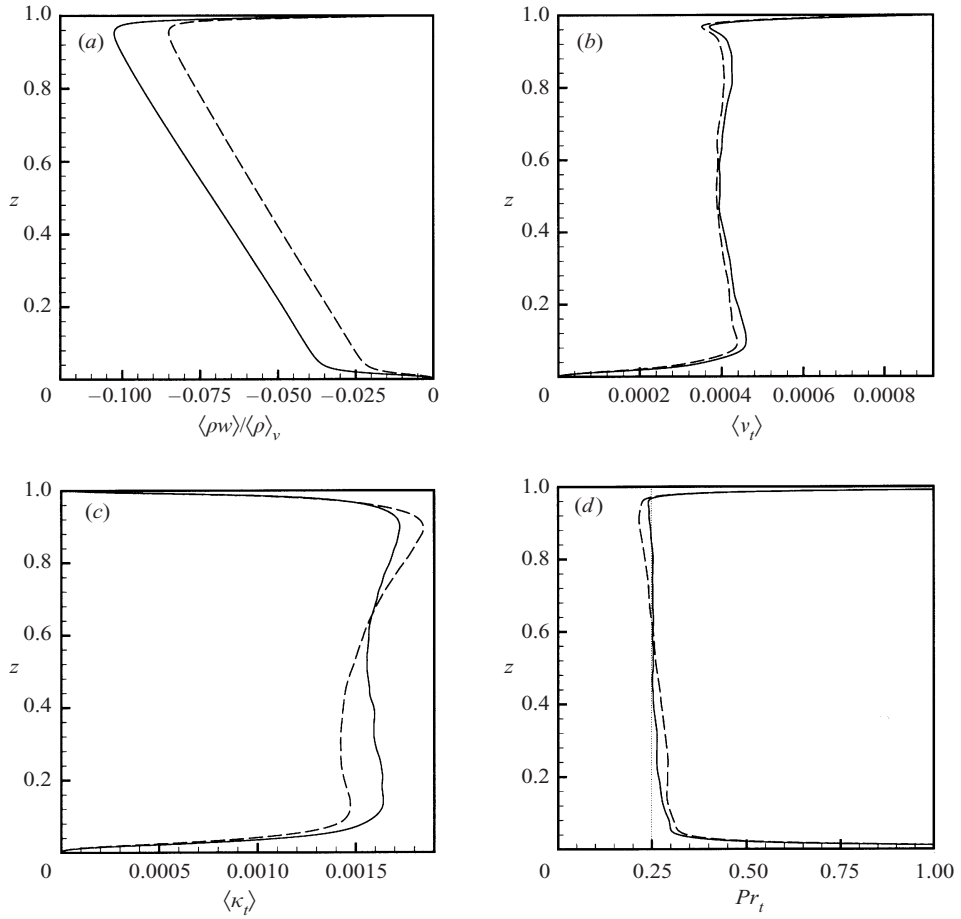

FIGURE 10. Time-averaged profiles of normalized convective buoyancy flux (*a*), eddy viscosity (*b*), eddy diffusivity (*c*), and turbulent Prandtl number (*d*). ———, Calculations with $Ri = 2$; – – –, calculations with $Ri = 10$. Dotted curve in (*d*) is for abscissa 0.25.

eddy diffusivity $\langle \kappa_t \rangle$, and turbulent Prandtl number $Pr_t = \langle \nu_t \rangle / \langle \kappa_t \rangle$ calculated using the dynamic SGS closure as discussed in § 2.2. We would like to stress that, in the simulations, ν_t and κ_t are determined independently of one another as functions of time and all three spatial coordinates. The curves in figure 10(*b–d*) are results of *a-posteriori* time and horizontal averaging.

One can see that the profiles are in agreement with the structure of the flow. Both $\langle \nu_t \rangle$ and $\langle \kappa_t \rangle$ are approximately constant in the core flow where the intensity of turbulent fluctuations is nearly uniform. A very important attribute is that the dynamic model provides the correct behaviour of eddy coefficients in the boundary layers. The eddy diffusivity vanishes in the upper and lower density boundary layers, where molecular diffusion dominates over turbulent convective flux. The same is true for the eddy viscosity in the shear boundary layer near the bottom. On the other hand, at the upper surface, where strong turbulent fluctuations are observed, the eddy viscosity reaches its maximum.

An interesting result was obtained for the turbulent Prandtl number. It can be seen in figure 10(*d*) that, except in the boundary layers, Pr_t is nearly constant and can be approximated as $Pr_t \approx 0.25$. This estimate is certainly in contradiction with the range

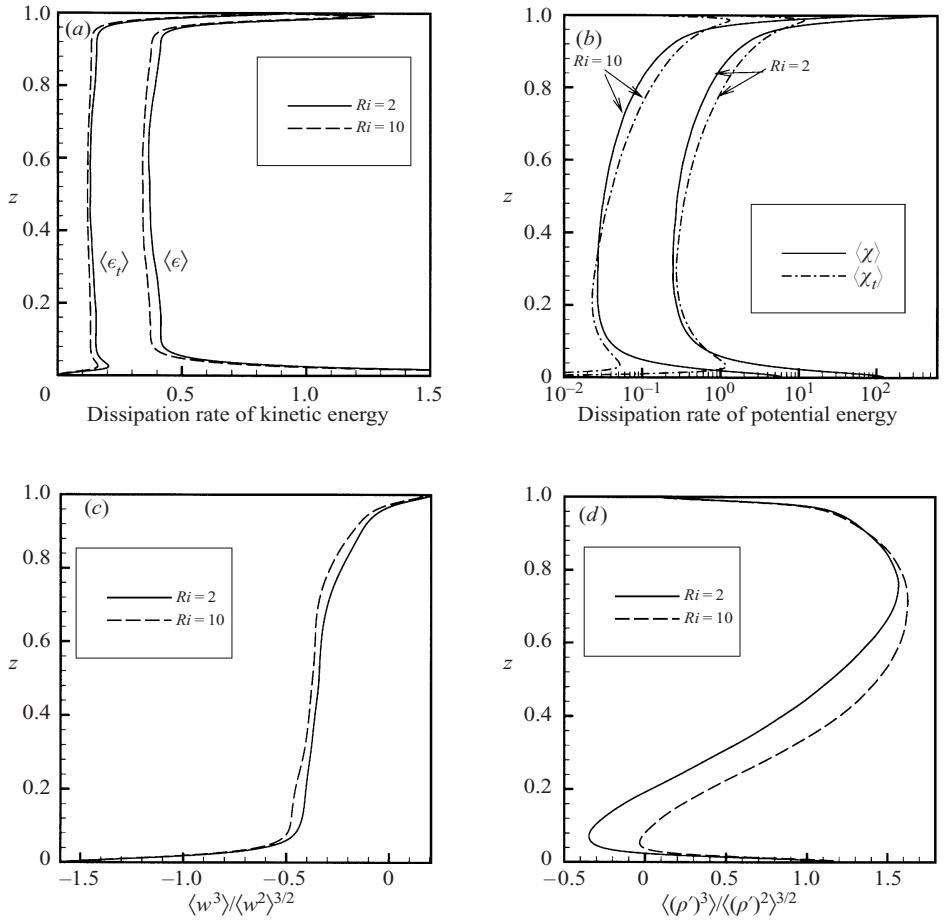

FIGURE 11. Time-averaged profiles of resolved and SGS dissipation rate of kinetic energy (a), resolved and SGS dissipation rate of potential energy (b), vertical velocity skewness (c), and skewness of the density fluctuations $\rho' = \rho - \langle\rho\rangle$ (d).

$1/3 < Pr_t < 1/2$ usually accepted for the classical Smagorinsky model (see §4 for further discussion).

Figure 11(a) shows vertical profiles of resolved and SGS dissipation rates. The curves obtained with $Ri = 2$ and $Ri = 10$ are very close, which again suggests that velocity fluctuations in a developed turbulent flow are insensitive to the initial stratification. Further, we observe that, similar to other types of convection in horizontal layers, both $\langle\epsilon\rangle$ and $\langle\epsilon_t\rangle$ profiles are nearly uniform in the core flow. The dissipation rate at the resolved scales is about three times larger than the modelled dissipation rate. Within the shear boundary layer near the bottom, SGS dissipation vanishes after a small peak. The resolved dissipation rate grows strongly and reaches the maximum value at the wall, where it is more than 20 times larger than in the core flow. Near the upper surface, both $\langle\epsilon\rangle$ and $\langle\epsilon_t\rangle$ grow considerably.

The profiles of resolved and modelled dissipation rates of the potential energy are presented in figure 11(b). In the core flow, the profiles are asymmetric. The values of $\langle\chi\rangle$ and $\langle\chi_t\rangle$ decrease with depth following the decrease in the intensity of the density fluctuations. It must be stressed, however, that the core region is responsible for only a minor part of the dissipation. Both $\langle\chi\rangle$ and $\langle\chi_t\rangle$ become much larger as we

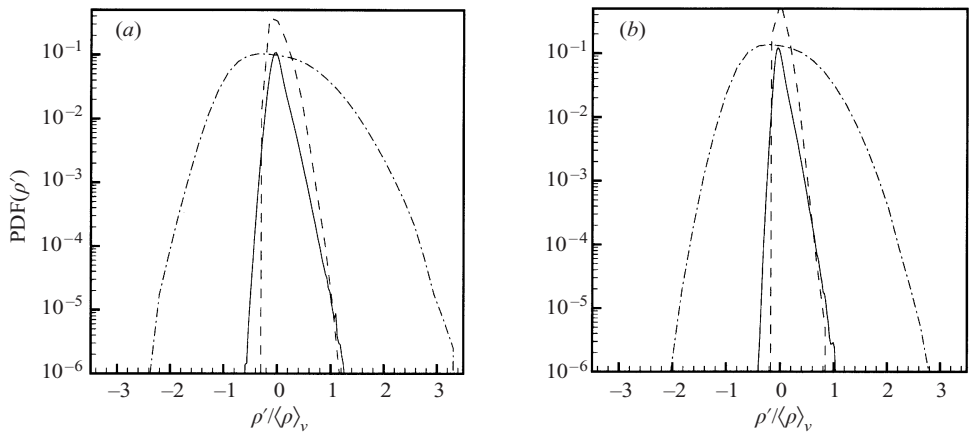

FIGURE 12. Probability density functions of the normalized density fluctuations $\rho'/\langle\rho\rangle_v = (\rho-\langle\rho\rangle)/\langle\rho\rangle_v$ calculated in different horizontal cross-sections. ——, $z = 0.006L_z$; ———, $z = 0.5L_z$; – · – · –, $z = 0.994L_z$. $Ri = 2$ (*a*) and $Ri = 10$ (*b*).

approach the density boundary layers near the top and bottom boundaries. Within the boundary layers, $\langle\chi_t\rangle$ vanishes, while $\langle\chi\rangle$ grows and reaches values that are two or three orders of magnitude larger than in the core flow.

As was discussed in earlier works (see e.g. Willis & Deardorff 1974), information about the skewness of vertical velocity and density (temperature) fields is of fundamental importance for understanding the properties of turbulent convection. Positive or negative skewness means more intense and frequent occasional large excursions of the field variable in, correspondingly, positive or negative directions. For example, the dynamics of the atmospheric planetary boundary layer is dominated by strong ascending thermal plumes. Accordingly, positive values of the skewness $\langle w^3\rangle/\langle w^2\rangle^{3/2}$ of vertical velocity components were detected in measurements and simulations (see e.g. Lenschow, Wingaard & Pennel 1980 and Moeng & Rotunno 1990). In the Rayleigh–Bénard flow, the symmetry of ascending and descending plumes with respect to the mid-plane results in a vertical velocity skewness profile that is antisymmetric with respect to this plane (Willis & Deardorff 1974 and Kerr 1996).

The results of our calculations are presented in figure 11(*c*, *d*). The vertical velocity skewness in figure 11(*c*) is negative in most of the flow domain. Since the negative skewness can be considered as an indication of localized areas of strong negative velocity, we may conclude that the vertical velocity field is dominated by localized descending plumes. Another interesting observation can be made from the closeness of the curves for $Ri = 2$ and $Ri = 10$ in figure 11(*c*): exactly as velocity fluctuations and dissipation rates, the third moment of the vertical velocity distribution is insensitive to the initial stratification.

The skewness profiles of density fluctuations $\rho' = \rho - \langle\rho\rangle$ shown in figure 11(*d*) have the Z-shape with thin boundary layers near the top and bottom boundaries that resemble the profiles obtained by AFB86. They are also similar to the profiles found in Rayleigh–Bénard flow with one important distinction: contrary to the Rayleigh–Bénard flow, where the profiles are antisymmetric with respect to the mid-plane, the profiles in figure 11(*d*) are shifted toward positive ρ'. This supports our conclusion that the flow is dominated by spatially localized descending cold plumes. The only region where the ascending plumes are more pronounced so that the density distribution is negatively skewed is just above the bottom boundary layer.

Further insight into the statistical properties of the density fluctuations can be obtained from figure 12. It shows the probability density functions of $\rho' = \rho - \langle\rho\rangle$ computed in the horizontal planes near the bottom ($z = 0.006L_z$), in the middle of the domain ($z = 0.5L_z$), and within the upper boundary layer ($z = 0.994L_z$). The data were collected during the same periods of time as the data used for the time-averaged profiles in figures 9–11. In order to eliminate the weighting effect of the net growth of density perturbations we normalized ρ' using the volume-averaged density $\langle\rho\rangle_v$ calculated at the same instant of time.

It can be seen that, in agreement with figure 11(*d*), the p.d.f.s are positively skewed, i.e. they have more extended positive than negative tails. The distributions calculated in the middle of the domain have distinct exponential tails. This suggests the presence of persistent coherent structures in the flow, which are, of course, turbulent thermal plumes.

Another remarkable property of the curves in figure 12 is that the distributions just below the upper surface have much wider extending tails than the distributions in the middle of the domain or within the bottom boundary layer. This implies much stronger density fluctuations near the upper surface, the phenomenon already illustrated in figures 9(*d*) and 8(*a–c*).

4. Comparison between DNS and LES

A separate set of numerical experiments was carried out to evaluate the performance of the dynamic model in simulation of turbulent penetrative convection. Below we discuss *a-posteriori* tests of the model. The results of dynamic LES simulations are compared with the DNS results and with the results of computations using the classical Smagorinsky model with fixed turbulent Prandtl number.

For the test calculations, the horizontal size of the computational domain was reduced to $L_x = L_y = L_z$. The reduction was necessary to make possible DNS at the same Reynolds number as in the main LES runs discussed earlier. We realize that the small aspect ratio suppresses the large-scale circulation and, thus, does not offer a direct evaluation of the accuracy with which our LES model simulates this particular aspect of the flow. We believe, however, that since the largest-scale motions are well resolved in LES, their behaviour is modelled reasonably well provided the flow dynamics at smaller scales are reproduced accurately. The latter is the subject of tests presented in this section.

In the vertical direction, we used the same clustered computational grid of 150 nodes as in the main calculations. The horizontal resolution was 128^2 in the DNS run and 32^2 in LES runs. The non-dimensional parameters were $Re = 1200$, $Ri = 2$, and molecular Prandtl number $Pr = 1$.

The DNS run was initialized in exactly the same way as the two main LES runs discussed above, i.e. with infinitesimal random velocity and unperturbed stably stratified density distribution. It was continued well into the stage of developed turbulent flow, the total duration being $T = 16.36$. The DNS flow fields obtained at $t = 8.34$ were filtered in the horizontal directions to the grid 32×32 and used as the initial condition for the LES runs.

Two LES runs were performed, one using the dynamic model and the other with the classical Smagorinsky model. In the latter, the components of the SGS stress tensor and density flux are given by (26) and (27). The eddy viscosity and diffusivity are defined as

$$\nu_t = (C\bar{\Delta})^2(2\bar{S}_{ij}\bar{S}_{ij})^{1/2}, \quad \kappa_t = \nu_t/Pr_t, \tag{42}$$

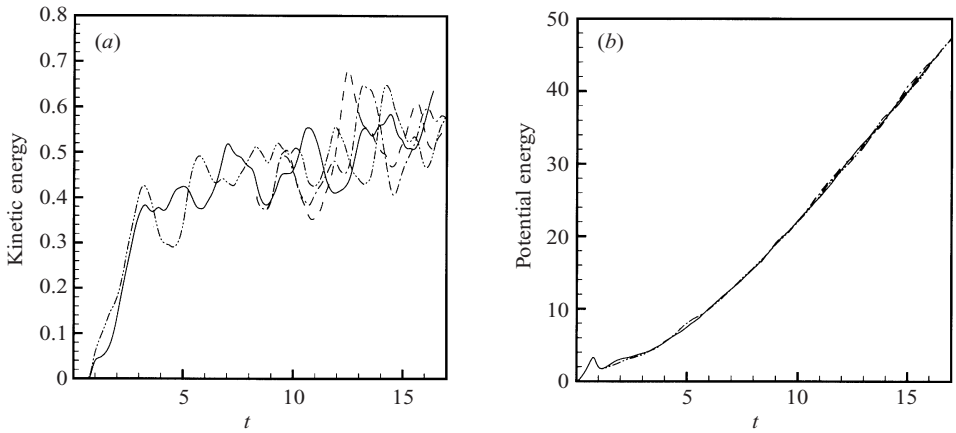

FIGURE 13. Volume-averaged kinetic (*a*) and potential (*b*) energies (33) as functions of time. ———, DNS run; — — —, dynamic LES run starting at $t = 8.34$; – · – · – · –, Smagorinsky LES run with $Pr = 0.4$; – ·· – ·· – ·· –, dynamic LES run starting at $t = 0$.

where $C = \pi^{-1}(\frac{2}{3}C_k)^{3/4}$ and $C_k = 1.5$ is the Kolmogorov constant. The prescribed turbulent Prandtl number Pr_t in (42) is, typically, assumed to be in a range between $1/3$ and $1/2$ (see e.g. Eidson 1985). Our calculations were performed with $Pr_t = 0.4$.

As was discussed above, an important feature of the dynamic approach is that it provides a tool to simulate transitional laminar–turbulent flows. This ability has already been exploited in this paper. However, one must recognize that a crude computational grid used in LES may fail to resolve fine structures, whose development determines the instability, and produce an irrelevant model of flow evolution. As applied to our flow, the LES grid might be incapable of adequate representation of small-scale plumes generated at the initial stage of the flow.

To investigate the possible influence of the poor resolution at this stage on the general flow evolution, an additional dynamic LES run was performed. This run started just as a DNS run, i.e. at $t = 0$ with infinitesimal velocity and zero density perturbations. The horizontal resolution and flow parameters were the same as in the other LES runs.

The results of calculations are illustrated in figures 13–15. One can see in figure 13 that the time evolution of flow energy is reproduced rather well in all LES runs. The potential energy curves practically collapse into one curve. For the kinetic energy, individual fluctuations differ considerably between the runs, but the long-time evolution as well as the typical time scale and amplitude of the fluctuations are very similar.

We performed visualizations of DNS and LES solutions and found that, at the initial stage, the horizontal LES grid does not suffice for accurate resolution of the small-scale plumes generated by the flow instability. As a result, slightly larger (about 50%) plumes develop in the LES than in the DNS flow. The subsequent evolution of the plumes, generation of developed turbulent flow, and formation of the large-scale coherent structure were found unaffected by the lack of horizontal resolution. The flows in DNS and all LES runs were very similar regarding their general appearance, intensity, and typical time and length scales. The fact that the kinetic energy curves in figure 13(*a*) still deviate from one another at the turbulent stage can be explained by the poor resolution of small-scale fluctuations in the LES runs. This, of course, affects

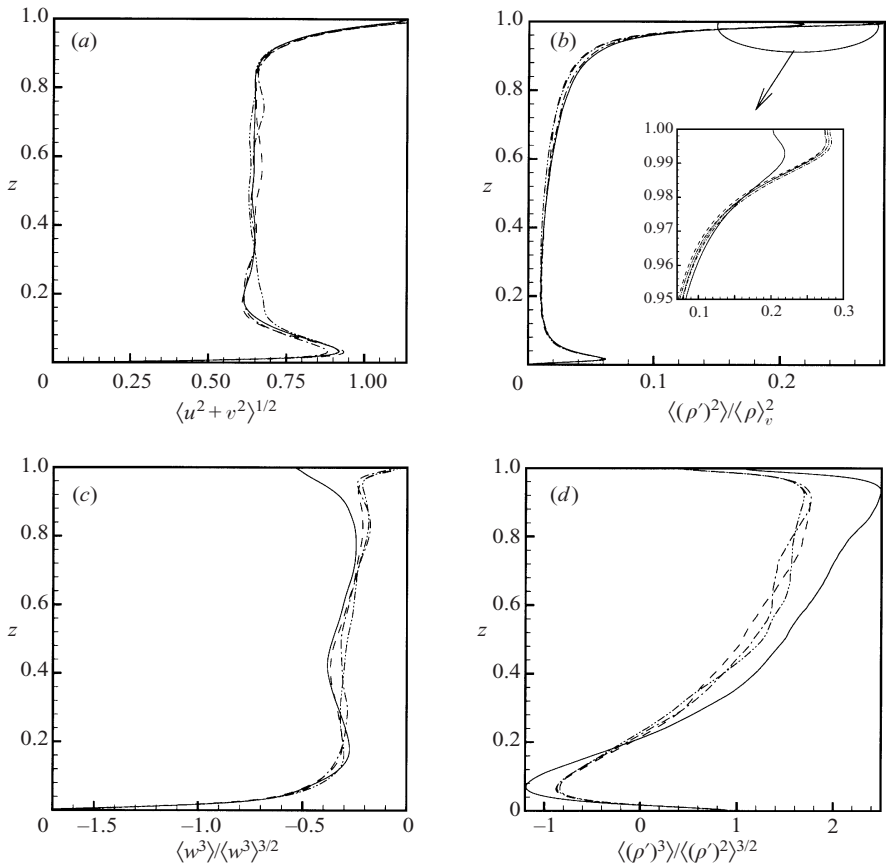

FIGURE 14. Time and horizontally averaged profiles of r.m.s. horizontal velocity (*a*), normalized density variance (*b*), vertical velocity skewness (*c*), and density variance skewness (*d*). Time averaging is at $8.34 < t < 16.36$. ———, DNS run; – – –, dynamic LES run starting at $t = 8.34$; – · – · – ·, Smagorinsky LES run with $Pr = 0.4$; – ·· – ·· – ··, dynamic LES run starting at $t = 0$.

the exact path traversed by the evolution of individual large plumes dominating the flow.

Further comparison between DNS and LES computations is made in figure 14 that shows time and horizontally averaged vertical profiles of the root-mean-square horizontal velocity and density fluctuations, and of the vertical velocity and density skewness. It can be seen that the LES curves are very close to the DNS curves. Similar agreement was found for profiles of other flow properties such as root-mean-square vertical velocity, density, or convective buoyancy flux. The only sensible divergence between LES and DNS was detected in the profiles of second and third moments close to the free surface (see figure 14*b–d*). The explanation of this is the inability of the LES computational grid to properly resolve the small-scale features of the velocity and density fluctuations associated with descending liquid sheets generated near the free surface.

Figures 13 and 14 do not provide the information that would allow us to contrast the performance of dynamic and Smagorinsky SGS models. At the numerical resolution and Reynolds number used in the computations, both models perform equally well. The difference becomes visible if we compare the SGS quantities. For example,

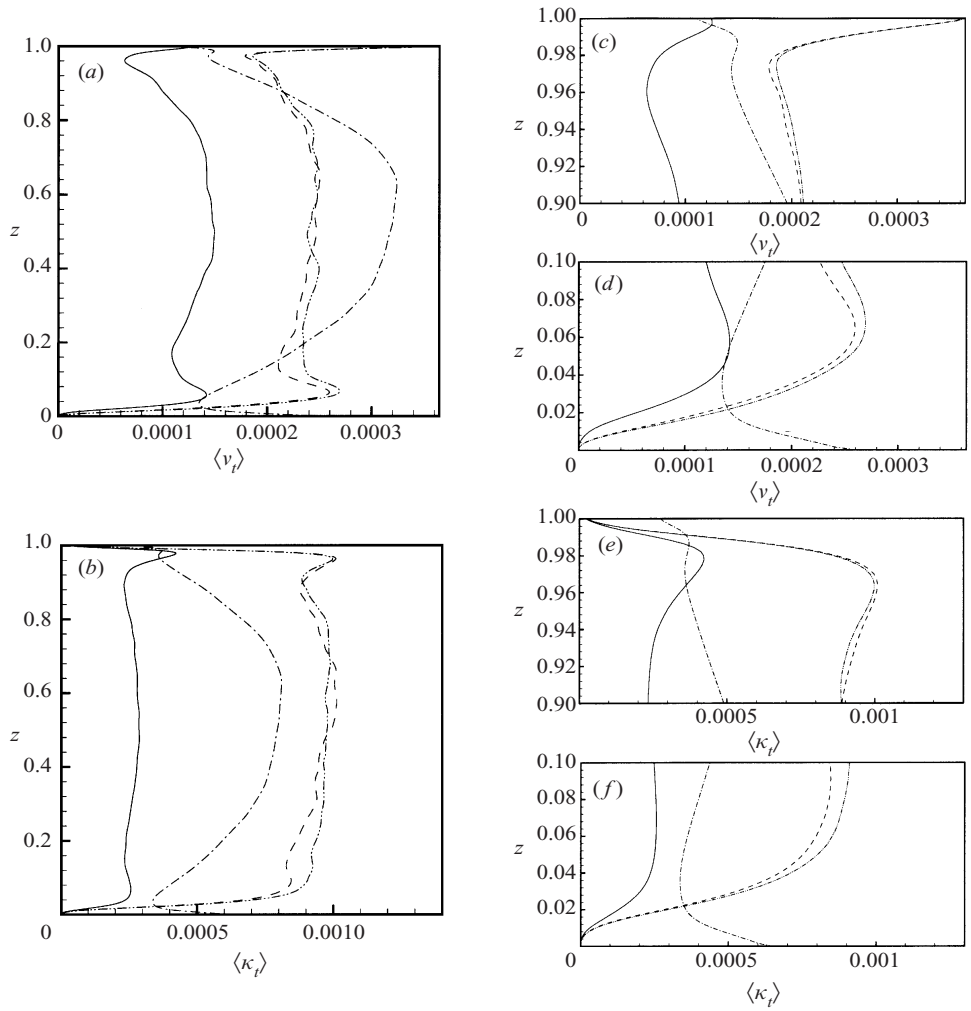

FIGURE 15. Time and horizontally averaged profiles of eddy viscosity coefficient v_t (a) and eddy diffusivity coefficient κ_t (b). Plots (c)–(f) are magnifications of (a) and (b) near the upper and lower boundaries. Time averaging is at $8.34 < t < 16.36$. ———, DNS run; — — —, dynamic LES run starting at $t = 8.34$; – · – · –, Smagorinsky LES run with $Pr = 0.4$; – · · – · · –, dynamic LES run starting at $t = 0$.

figure 15 shows profiles of eddy viscosity and eddy diffusivity coefficients. In the DNS run, we estimate v_t and κ_t after each time step filtering the velocity and density fields to a horizontal grid with the step $\bar{\Delta} = 4\Delta$, evaluating the SGS stresses τ_{ij} and $\tau_{\rho j}$ as in (24) and (25), and computing

$$v_t = -\frac{1}{2}\frac{(\tau_{ij} - \delta_{ij}\tau_{kk}/3)\bar{S}_{ij}}{(\bar{S}_{ij})^2}, \qquad \kappa_t = -\frac{\tau_{\rho i}\partial\bar{\rho}/\partial x_i}{(\partial\bar{\rho}/\partial x_i)^2}.$$

The magnitude of the model coefficients both for the Smagorinsky and the dynamic model is larger than the values found in the DNS. Such a difference is typical for *a-posteriori* tests of the closure models (see e.g. Kimmel & Domaradzki 2000). What gives the dynamic model an advantage is that it provides the physically justified spatial behaviour of the model coefficients and other SGS quantities. Figure 15 clearly

demonstrates the similarity between the shapes of profiles of v_t and κ_t produced by the dynamic model and obtained in the DNS. The dynamic model reproduces nearly uniform distributions of v_t and κ_t in the core flow and correct behaviour in the boundary layers. Both in DNS and dynamic calculations, v_t vanishes in the bottom shear boundary layer and grows near the upper surface (see figures 15*c* and 15*d*), while the eddy diffusivity κ_t tends to zero in both density boundary layers (figures 15*e* and 15*f*). In contrast, the spatial behaviour of the coefficients obtained using the Smagorinsky closure is significantly different from that observed in the DNS.

A similar picture was observed for the SGS dissipation of kinetic and potential energy (not shown here). Spatially similar profiles of ϵ_t and χ_t were obtained in DNS and dynamic LES runs but not in the run with the Smagorinsky model.

A comment is in order regarding the value of the turbulent Prandtl number $Pr_t \approx 0.25$ obtained in the dynamic LES. DNS computations produced a value of Pr_t in the core flow which was closer to the traditional value of 0.5. The conclusion is that the 0.25 value is specific to the scaling version of the dynamic model.

Summarizing the results presented in this section, we may say that, at a moderate Reynolds number, the comparison between LES and DNS did not reveal any specific advantages of the dynamic model over the classical Smagorinsky closure in the sense of modelling of grid-scale flow characteristics. However, the scaling version of the dynamic model demonstrated its ability to follow more closely the proper spatial behaviour of SGS quantities both for the velocity and density fields. Therefore, we can expect that the dynamic model will provide better results than the Smagorinsky model at larger Reynolds number.

5. Concluding remarks

In this paper, we have presented the results of numerical simulations of turbulent convection generated by surface cooling in a layer of finite depth. We applied the LES method based on a dynamic SGS closure and verified the computations by comparison with the DNS results.

The flow evolution associated with the surface cooling consists of two principal phases: that of initial development characterized by the primary instability of the conductive surface layer and generation of descending thermal plumes, and that of developed turbulent convection. During the second phase, the flow attains the form of a well-mixed core with thermal and velocity boundary layers at the top and bottom boundaries.

It has been found that in spite of flow unsteadiness (continuously growing volume-averaged potential and kinetic energy) the spatial structure does not change with time after the turbulence becomes fully developed.

One of the most important conclusions that can be reached on the basis of our simulations is that only the first phase of the flow evolution is affected by the initial stable stratification. During the second phase, the flow 'forgets' the stratification. Comparison between two runs with the Richardson numbers differing by a factor of five indicates that the properties of developed turbulence are insensitive to the strength of stratification. We may assume that similar results could be obtained in an initially neutrally stratified layer.

The spatial structure and other properties of the flow can be best appreciated in comparison with other well-studied turbulent flows in horizontal layers such as the Rayleigh–Bénard flow, the planetary boundary layers, convection driven by internal heat sources, or flow between heated and insulated rigid plates. As expected, the

computations revealed that convection driven by surface cooling in shallow water possesses all the generic features of the family. In particular, we clearly detected such effects as thermal plume generation, development of a well-mixed core region, generation of velocity boundary layers by plumes hitting the rigid wall, and a tendency toward establishment of a large-scale circulation pattern.

The computations also revealed distinctive features of the flow, such as a conductive boundary layer near the free surface and flow asymmetry with respect to the mid-plane. Close to the free surface, the flow is characterized by intense turbulent fluctuations of the density field and strong surface currents generated by the combined action of liquid sheets and plumes descending from the top boundary and plumes ascending from the bottom. This part of the flow clearly resembles other convective flows with a free surface such as the granulated solar convection or convection driven by surface evaporation.

The asymmetry of flow properties with respect to the mid-plane was demonstrated by visualization of density and velocity fields, horizontally averaged vertical profiles, and probability density functions. It has been shown that the turbulent flow is dominated by a pattern of descending thermal plumes. The analogous pattern of ascending plumes is less organized and characterized by considerably weaker coherent fluctuations of density and vertical velocity. This property of our system places it halfway between the completely asymmetric flows such as the planetary boundary layer or the flow considered in AFB86, where the plumes are generated on one surface only, and the completely symmetric Rayleigh–Bénard system, where the plumes are generated equally on both sides.

It is necessary to stress that our computations do not allow us to reach any ultimate conclusions regarding the persistence and specific shape of the large-scale circulation pattern in the real convective flow. The calculated velocity and density fields illustrated in figures 6(*b*) and 8 indicate that such a pattern might exist. One must take into account, however, that, as shown by horizontal correlations in figure 7, the largest scales of the computed flow are affected by the periodic boundaries. Further computations with significantly larger aspect ratio of the computational domain are needed to resolve this issue.

We would like to make a comment regarding the unsteady character of the flow. As was discussed earlier in the paper, the average density of the layer increases continuously because the imposed heat flux at the top boundary is not fully balanced by the heat flux induced by the temperature difference between the cooled interior and the isothermal bottom. Remarkably, as soon as the stage of developed turbulence is achieved, the effect of unsteadiness reduces almost completely to cooling of the layer as a whole. The impact on the dynamics of turbulent motions is very limited.

Careful visualization of horizontally averaged density profiles have shown that neither the slope in the core region nor the thickness of the thermal boundary layers vary with time. The profile of r.m.s. vertical velocity fluctuations $\langle w^2\rangle^{1/2}(z)$ remains virtually unchanged. It can be seen in figure 3 that the total kinetic energy in the horizontal velocity components experiences certain growth over the period of developed turbulence (about 50% in terms of r.m.s. value). Visualization of the evolution of the profile $\langle u^2 + v^2\rangle^{1/2}(z)$ revealed that the growth is distributed homogeneously over the depth, so that the shape of the profile does not change with time. We were unable to detect a particular mechanism of this growth. It can be related to development of the system of ascending thermal plumes or to evolution of the large-scale circulation pattern.

More comments are in order on the possible effect of the alternative density

boundary condition at the lower boundary. It was discussed in the introduction that both the isothermal and adiabatic conditions may serve as approximations of the actual ocean bottom. Further investigations of this subject are necessary. At this point, we can only mention that the adiabatic condition would render the system more similar to the system studied in AFB86, i.e. a layer with one heated (or cooled) and one insulated boundary. Such a flow would be completely dominated by descending thermal plumes with corresponding consequences for spatial and statistical properties. Furthermore, the flow unsteadiness would manifest itself as a constant linear growth of the density in the entire layer while H_0 remained constant.

Apart from understanding the flow properties, our goal in this paper was to evaluate the performance of the scaling version of the dynamic SGS closure proposed by WL94. The subgrid-scale model was applied in the horizontal directions only, the flow being fully resolved in the vertical direction. This allowed us to avoid the problems associated with the modelling of boundary layers but limited the computations to cases with moderate Reynolds number, where most of the flow scales are resolved in a direct fashion. The moderate Reynolds number was the reason why the comparison with DNS results has not allowed us to draw an ultimate conclusion about possible advantages of the dynamic closure over the classical Smagorinsky method. Mean velocity and density distributions obtained with both the closures agree nicely with DNS computations. However, the dynamic closure has demonstrated its advantage in reproducing more physically justified patterns of eddy coefficients and SGS dissipation of kinetic and potential energy. Therefore, one can anticipate better performance of the dynamic closure at the higher Reynolds numbers typical of realistic ocean flows.

This work was supported by the US Office of Naval Research (grant N00014-00-1-0218, Program Manager: Dr Tom Curtin). The authors thank the referees for careful reading of the manuscript and useful comments.

REFERENCES

Adrian, R. J., Ferreira, R. T. D. S. & Boberg, T. 1986 Turbulent thermal convection in wide horizontal fluid layers. *Exps. Fluids* **4**, 121–141 (referred to herein as AFB86).

An, E., Dhanak, M. R., Shay, L. K., Smith, S. & Van Leer, J. 2001 Coastal oceanography using a small AUV. *J. Atmos. Sci. Ocean Techn.* **18**, 215–234.

Brummel, N., Cattaneo, F. & Toomre J. 1995 Turbulent dynamics in the Solar convective zone. *Science* **269**, 1370.

Cabot, W. 1992 Large eddy simulations of time-dependent and buoyancy-driven channel flows. In *CTR Annual Research Briefs*, p. 45. Stanford University.

Chu, T. Y. & Goldstein, R. J. 1973 Turbulent convection in a horizontal layer of water. *J. Fluid Mech.* **60**, 141–159.

Cioni, S., Ciliberto, S. & Sommeria, J. 1997 Strongly turbulent convection in mercury: comparison with results at moderate Prandtl number. *J. Fluid Mech.* **335**, 111–140.

Deardorff, J. W. & Willis, G. E. 1967 Investigation of turbulent thermal convection between horizontal plates. *J. Fluid Mech.* **28**, 675–704.

Denbo, D. W. & Skyllingstad, E. D. 1996 An ocean large-eddy simulation model with application to deep convection in the Greenland Sea. *J. Geophys. Res.* **101**, 1095–1111.

Domaradzki, J. A. & Metcalfe, R. W. 1988 Direct numerical simulations of the effects of shear on turbulent Rayleigh–Bénard convection. *J. Fluid Mech.* **193**, 499–531.

Eidson, T. M. 1985 Numerical simulation of the turbulent Rayleigh–Bénard problem using subgrid modelling. *J. Fluid Mech.* **158**, 245–268.

Germano, M., Piomelli, U., Moin, P. & Cabot, W. H. 1991 A dynamic subgrid-scale eddy viscosity model. *Phys. Fluids* A **3**, 1760–1765.

GRÖTZBACH, G. 1983 Spatial resolution requirements for direct numerical simulation of the Rayleigh–Bénard convection. *J. Comput. Phys.* **49**, 241–264.

KERR, R. M. 1996 Rayleigh number scaling in numerical convection. *J. Fluid Mech.* **310**, 139–179.

KIMMEL, S. J. & DOMARADZKI, J. A. 2000 Large eddy simulations of Rayleigh–Bénard convection using subgrid scale estimation model. *Phys. Fluids* **12**, 169–184.

KOLMOGOROV, A. N. 1941 The local structure of turbulence in incompressible viscous fluid for very large Reynolds number. *Dokl. Acad. Nauk SSSR* **30**, 299–303.

KRISHNAMURTI, R. & HOWARD, L. N. 1981 Large-scale flow generation in turbulent convection. *Proc. Natl Acad. Sci.* **78**, 1981–1985.

KULACKI, F. A. & EMARA, A. A. 1977 Steady and transient thermal convection in a fluid layer with uniform volumetric energy sources. *J. Fluid Mech.* **83**, 375–395.

LELE, S. K. 1992 Compact finite difference schemes with spectral-like resolution. *J. Comput. Phys.* **103**, 16–42.

LENSCHOW, D. H., WYNGAARD, J. C. & PENNELL, W. T. 1980 Mean-field and second-moment budget in a baroclinic convective boundary layer. *J. Atmos. Sci.* **37**, 1313–1326.

MARSHALL, J. & SCHOTT, F. 1999 Open-ocean convection: observations, theory, and models. *Rev. Geophys.* **37**, 1–64.

MAXWORTHY, T. 1997 Convection into domains with open boundaries. *Annu. Rev. Fluid Mech.* **29**, 327–71.

MOENG, C. H. & ROTUNNO, R. 1990 Vertical-velocity skewness in the buoyancy-driven layer. *J. Atmos. Sci.* **47**, 1149–1162.

MOIN, P. & MAHESH, K. 1998 Direct numerical simulation: A tool in turbulent research. *Annu. Rev. Fluid Mech.* **30**, 539–578.

SAYLOR, J. R., SMITH, G. B. & FLACK, K. A. 2000 An experimental investigation of the surface temperature field during evaporative convection. *Phys. Fluids* **13**, 428–439.

SCHMIDT, H. & SCHUMANN, U. 1989 Coherent structure of the convective boundary layer derived from large-eddy simulations. *J. Fluid Mech.* **200**, 511–562.

SCHUMANN, U. 1975 Subgrid scale model for finite difference simulations of turbulent flows in plane channels and annuli. *J. Comput. Phys.* **18**, 376–404.

SLINN, D. N. & RILEY, J. 1998 A model for the simulation of turbulent boundary layers in an incompressible stratified flow. *J. Comput. Phys.* **144**, 550–602.

SULLIVAN, P. & MOENG, C.-H. 1992 An evaluation of the dynamic subgrid scale model in buoyancy driven flows. In *Proc. 10th Symp. on Turbulence and Diffusion, Portland, Oregon*, p. 82.

WILLIS, G. E. & DEARDORFF, J. W. 1974 A laboratory model of diffusion into the convective planetary boundary layer. *Q. J. R. Met. Soc.* **102**, 427–445.

WONG, V. C. & LILLY, D. K. 1994 A comparison of two dynamic subgrid closure methods for turbulent thermal convection. *Phys. Fluids* **6**, 1016–1023 (referred to herein as WL94).